CYCLOTRON LINE FORMATION IN A RADIATION-DRIVEN OUTFLOW

MICHAEL ISENBERG AND D. Q. LAMB

Department of Astronomy and Astrophysics, University of Chicago, 5640 South Ellis Avenue, Chicago, IL 60637

AND

JOHN C. L. WANG

Department of Astronomy, University of Maryland, College Park, MD 20742-2421

ABSTRACT

We calculate the properties of gamma-ray burst spectral lines formed by resonant cyclotron scattering in a radiation-driven outflow. Most previous models of line formation in gamma-ray bursts are appropriate at the polar cap of a neutron star located no further than several hundred parsecs away. However, the BATSE brightness and sky distributions indicate that, if bursters are galactic, they are located in a corona at distances greater than 100 kpc. At these distances, the burst luminosity exceeds the Eddington luminosity and the plasma in a polar line-forming region is ejected along the field lines. The variation of the magnetic field strength and plasma velocity with altitude in such an outflow would seem to prevent the formation of narrow features like those observed by *Ginga* and other instruments. However, this is not the case because the majority of scatters occur close to the stellar surface, at altitudes below $z \approx r_h$, where $r_h \sim 10^5$ cm is the size of the photon source. Consequently, the interpretation of the observed features as cyclotron lines does not rule out burst sources in a galactic corona.

The outflow model predicts both absorption-like and single-peaked emission-like features. The latter do not occur in models with static line-forming regions but have been observed in gamma-ray bursts by the KONUS and BATSE instruments.

Subject headings: Galaxy: halo — gamma rays: theory — line: formation — plasmas — radiation mechanisms: nonthermal

1. INTRODUCTION

The source of gamma-ray bursts is one of the most hotly debated questions in astrophysics (Lamb 1995; Paczynski 1995). These short, intense bursts of high-energy radiation were first observed by the *Vela 3* and *Vela 4* satellites on 1967 July 2 (Klebesadel et al. 1973; Bonnell & Klebesadel 1996). Today, the main question continues to be the distance to the sources–are they galactic or cosmological? Interest in this mystery has intensified in recent months as a result of the hard gamma-ray repeater candidate of 1996 October 27–29 and the spectacular follow-up observations to gamma-ray burst GRB 970228. The 1996 October observations are a sequence of four events over a 2 day period with positions in the sky that are consistent with a single source (Meegan et al. 1996). They are the best evidence to date that burst sources can repeat and that, therefore, bursting does not necessarily lead to the destruction of the source. X-ray and optical observations of the GRB 970228 field offer the best candidates to date for burst counterparts in other wavelengths. These observations reveal a transient X-ray source (Costa et al. 1997), a transient optical point source (Groot et al. 1997a), and an extended optical source (Groot et al. 1997b; Metzger et al. 1997a, 1997b; Sahu et al. 1997) whose positions in the sky are consistent with that of the burst and with each other.

One of the strongest pieces of evidence in favor of the galactic point of view is the observation of statistically significant absorption- and emission-like features in the spectra of some bursts and the interpretation of these features as cyclotron lines (Mazets et al. 1981, 1982; Lamb 1982; Bussard & Lamb 1982; Mazets et al. 1983; Hueter 1984; Hueter 1987; Murakami et al. 1988; Fenimore et al. 1988; Harding & Preece 1989; Wang et al. 1989; Alexander & Mészáros 1989; Lamb et al. 1989; Graziani et al. 1992;

Yoshida et al. 1992; Nishimura & Ebisuzaki 1992; Barat 1993; Nishimura 1994; Mazets et al. 1996; Briggs 1996; Briggs et al. 1996). Cyclotron lines are formed by the resonant scattering of photons by electrons in a magnetic field, B. The motion of free electrons perpendicular to the field is quantized into energy levels (Landau 1930; Ternov, Begrov, & Zhukovskii 1966),

$$E_e = \sqrt{1+2nb}\, m_e c^2 , \qquad (1)$$

where n is an integer ≥ 0, $b \equiv B/B_c$, $B_c = 4.414 \times 10^{13}$ G is the critical field where the cyclotron energy $E_B \equiv b m_e c^2 = 11.6 B_{12}$ is equal to the electron rest energy, and $B_{12} \equiv B/10^{12}$ G. When $b \ll 1$, the energy level spacing is approximately harmonic, i.e., $E_e \approx m_e c^2 + n E_B$. Photons that possess the right energy to excite an electron to a higher Landau level can scatter resonantly into or out of the line of sight, producing spectral features.

Although the observation of spectral features in gamma-ray bursts and their interpretation continue to be controversial, the existence of Landau levels and the formation of cyclotron lines in the spectra of *persistent* astrophysical sources with strong magnetic fields are well established experimentally. The quantization of electron energies in metals is responsible for the de Haas–van Alphen effect—the oscillation of magnetization with magnetic field strength (de Haas & van Alphen 1930). Cyclotron lines appear in the X-ray spectra of about a dozen accretion-powered pulsars (Mihara 1995; Makishima & Mihara 1992). These sources include Her X-1 (Trümper et al. 1978), 4U 0115+63 (Wheaton et al. 1979), 4U 1538−52 (Clark et al. 1990), and A0535+26 (Grove et al. 1995). Visvanathan & Wickramasinghe (1979) made the first detection of cyclotron lines from a white dwarf in infrared observations of the AM Her–type binary VV Puppis. Since then, cyclotron lines

have been detected in about a dozen AM Her binaries, including AM Her itself (for a review, see Chanmugam 1992). Comparing these observations with theoretical models of line-formation reveals much about the physical conditions in the line-forming region, including the magnetic field strength, the plasma density, and the temperature.

The lines reported in gamma-ray bursts are at energies ≈ 20–60 keV, corresponding to magnetic fields $B_{12} \approx 2$–6, consistent with a neutron star source. The *Ginga* satellite's observation of *harmonically spaced* features in three bursts strongly supports the cyclotron line interpretation. The features persist for as long as 9 s (Graziani et al. 1992). If the cyclotron line interpretation is correct, then the magnetic field must remain steady at least as long as the line is observed. The requirement of a steady field rules out some cosmological models, such as coalescing neutron stars, which require the catastrophic annihilation of the source.

Establishing that the observed features are indeed cyclotron lines requires comparing the observations with theoretical models that are appropriate for the physical conditions expected at the source. Most previous calculations of line formation in gamma-ray bursts, such as those of Wang et al. (1989), model the line-forming region as a static slab of plasma, threaded with a uniform magnetic field oriented perpendicular to the surface of the slab. Such a model is appropriate, for example, at the magnetic polar cap of a neutron star with a dipole field, located less than several hundred parsecs from the Earth. Lamb, Wang, & Wasserman (1990) show that for larger distances the static polar cap model is not valid; the burst luminosity exceeds the Eddington luminosity, and the radiation force creates a relativistic plasma outflow along the field lines.

However, in order to explain the burst brightness and sky distributions observed by BATSE, it has been suggested that, if the bursters are galactic, they are located in a galactic corona at distances of 100–400 kpc (for a review, see Lamb 1995). Two models have been suggested that are appropriate for these distances: an equatorial model and an outflow model.

In the equatorial model, the line-forming region is located at the magnetic equator, where field lines parallel to the stellar surface confine the plasma magnetically (see, e.g., Lamb 1982; Katz 1982; Zheleznyakov & Serber 1994, 1995). Freeman et al. (1996) fit both this model and a static polar cap one to the two observed spectra corresponding to the time intervals S1 and S2 during which lines are observed in GRB 870303. A joint fit to the two intervals, using models with a common magnetic field and column depth, but not a common viewing angle, marginally favors the equatorial model over the static polar cap one.

In the outflow model the radiation force on the plasma at the polar cap ejects the plasma relativistically along the field lines. Table 1 compares the existing calculations of the properties of cyclotron lines formed in such an outflow. The variation of magnetic field strength and plasma velocity with altitude would seem to prevent the formation of narrow scattering lines. However, Miller et al. (1991, 1992) show that narrow lines can be formed in an outflow at the second and third harmonics, which they approximate as due to cyclotron *absorption*. Chernenko & Mitrofanov (1993) calculate the properties of the first harmonic line, also approximating it as due to absorption, and find that the formation of a narrow line is possible. However, the absorption approximation is not valid for the first harmonic; multiple photon scatters must be taken into account. The first calculation to do so was Isenberg, Lamb, & Wang (1996) using a Monte Carlo radiative transfer code. This calculation includes multiple scattering at the first three harmonics in a plasma with electron temperature $k_B T = 0.25 E_B$. It shows lines with equivalent widths comparable to those observed by *Ginga*.

The emerging photon spectrum is very sensitive to the velocity profile $\beta_F(z)$—the bulk flow velocity as a function of the altitude z above the stellar surface. An electron with velocity β along the field is overtaken by photons with $\mu > \beta$, where $\mu = \cos \theta$ and θ is the angle between the photon's direction of travel and the magnetic field. In the electron's rest frame, these photons have orientations $\mu^r > 0$; scattering with them accelerates the electron. Similarly, photons with $\mu < \beta$ have rest frame orientations $\mu^r < 0$ and decelerate the electrons. Consequently, the three previous calculations assume that the flow velocity at a given altitude is approximately the mean value of the component of the photon velocity along the field; that is,

$$\beta_F(z) \approx \frac{\int \mu Q(\mu, z) d\mu}{\int Q(\mu, z) d\mu}, \qquad (2)$$

where $Q(\mu, z)$ is the angular distribution of photons at altitude z. This profile is a good approximation to the one Tsygan (1981) and Mitrofanov & Tsygan (1982, hereafter MT) derive from the radiation force $F_{rad}(z)$. Their derivation includes scattering at the first harmonic only, with $k_B T = 0$. It is based on the *unscattered* photon distribution; i.e., the calculation of the force at z does not take into account the reduction in photon flux near the line center or the angular redistribution of photons due to scattering at lower altitudes. This approximation is valid at small optical depths, but not at the depths required to reproduce the observed cyclotron lines. Miller et al. (1991, 1992) and Isenberg et al. (1996) also include processes in their radiation transfer calculations, such as higher harmonic scattering and finite temperature, which are not included in MT's calculation of

TABLE 1

SUMMARY OF CALCULATIONS OF CYCLOTRON LINE FORMATION IN RADIATION-DRIVEN OUTFLOWS ASSOCIATED WITH GAMMA-RAY BURSTS

Parameter	Miller et al. 1991, 1992	Chernenko & Mitrofanov 1993	Present Work
Process	Absorption	Absorption	Scattering
Continuum scattering......	No	No	Yes
Natural line width	0	Finite	Finite
Thermal broadening	Yes	No	Yes
Polarization	No	No	Yes
Self-consistency	No	No	Yes

$F_{\rm rad}$. Thus, in the earlier models, the hydrodynamics is not consistent with the radiation transfer.

In the current work, we present the first *self-consistent* calculations of the properties of cyclotron lines formed in an outflow. In addition to the physical processes included in Isenberg et al. (1996), we add continuum scattering, finite natural line width, and photon polarization. We describe the geometry and the physics of the line-forming region in §§ 2 and 3, respectively. The electron velocity profiles are discussed in § 4. We present the Monte Carlo spectra in § 5 and discuss their implications for gamma-ray bursts in § 6.

2. SPATIAL GEOMETRY OF THE LINE-FORMING REGION

We adopt a cylindrical line-forming region, as shown in Figure 1. Photons are injected at the base of the cylinder, which could correspond to a hot spot with radius r_h located on the surface of a neutron star. The angular size of the hot spot is represented by

$$\mu_o(z) = \cos\theta_o(z) = \frac{\tilde{z}}{(1 + \tilde{z}^2)^{1/2}}, \qquad (3)$$

where z is the altitude above the surface and the tilde indicates quantities measured in units of r_h.

We assume the star has a dipole magnetic field with strength B_o, where the subscript o indicates quantities measured at the stellar surface. We also assume that the hot spot is located on the stellar surface, at the magnetic pole. The field strength decreases with z according to

$$B = B_o\left(\frac{1}{1 + z/R_*}\right)^3, \qquad (4)$$

where R_* is the stellar radius. The field lines that are rooted in the hot spot form a tube with a circular cross section with radius $\tilde{r}(z)$. Conservation of magnetic flux requires that $\tilde{r}(z)$

FIG. 1.—Geometry of the line-forming region. Photons are injected at a hot spot with radius r_h located at the magnetic pole of a neutron star with dipole field B. They scatter with the electrons in the line-forming region, accelerating them along the field lines. β is the velocity of an individual electron, and $\beta_F(z)$ is the bulk velocity of the flow, where z is the altitude above the stellar surface. θ denotes the angle between the photon direction and the magnetic field direction. The angular size of the hot spot is $\theta_o(z)$.

increase with altitude according to

$$\tilde{r}(z) = \sqrt{\frac{B_o}{B(z)}} = \left(1 + \frac{z}{R_*}\right)^{3/2}, \qquad (5)$$

i.e., the field lines flare outward. For simplicity, we assume the field lines are parallel to the cylinder axis at all z; we ignore the flaring in our Monte Carlo simulations, except when calculating the plasma density. The characteristic distance for changes in $\tilde{r}(z)$ is $\sim (d\tilde{r}/dz)^{-1} \sim R_*$. But, as we shall show, few scatters occur above $z \sim r_h \ll R_*$. Therefore, the effect of this assumption on the emerging photon spectrum is negligible, since most of the scattering takes place close to the surface where $\tilde{r}(z)$ is approximately constant.

The line-forming region contains a plasma in which the number density of scatterers (electrons and positrons) is $n_e(z)$. The plasma can consist of ionized electron-proton pairs that have been swept up from the stellar surface or electron-positron pairs that have been created by the processes $\gamma \rightarrow e^-e^+$ and $\gamma\gamma \rightarrow e^-e^+$. Our Monte Carlo simulations assume the number of scatterers is conserved; i.e., the simulations apply to line-forming regions where electron-proton and electron-positron plasmas originate at the surface. The effects of pair creation and annihilation above the surface is beyond the scope of our current calculations (although see § 6 for a general discussion; see also Vitello & Dermer 1991; Coppi & Lamb 1992). Because the electron temperature $k_B T_e \ll E_B$, the electrons are restricted to move along the field lines (see § 3.2). As the photons travel through the plasma, they can scatter with the electrons (and positrons), accelerating them. We denote the velocity along the field lines of an individual electron (in units of c) by β and the bulk flow velocity by $\beta_F(z)$.

Photons that cross the lateral surface of the cylinder escape the line-forming region and reach the observer. In the absence of scattering, a photon injected at the origin escapes when $\mu_o(z) = \mu$. The resulting angular distribution of photons is

$$Q(\mu, z) = Q(\mu)\eta[\mu - \mu_o(z)], \qquad (6)$$

where $Q(\mu)$ is the angular distribution at the stellar surface and η is the unit step function. For simplicity, we use semi-isotropic injection $[Q(\mu) = 1]$ throughout the present work. Note, however, that some models of spectrum formation in gamma-ray bursts suggest that the photons are beamed along the field lines (see, e.g., Schmidt 1978; Baring & Harding 1993; Harding & Baring 1994; Harding 1994; § 6 below). This possibility should be considered in future calculations of line-formation in an outflow. Also note that the distribution given by equation (6) for photons injected at the origin of the hot spot is also the angular distribution along the cylinder axis when photons are injected uniformly across the disk. Substituting this distribution into equation (2) yields the approximate velocity profile

$$\beta_F(z) \approx \tfrac{1}{2}[1 + \mu_o(z)]. \qquad (7)$$

The few photons that reach $\tilde{z} > 30$ are also permitted to escape without further scatters; for $r_h \sim 0.1R_*$, the plasma is extremely tenuous above this altitude and the cyclotron energy is less than the energy threshold of most gamma-ray burst detectors. We assume that photons that scatter downward and return to the surface thermalize; i.e., they are absorbed by nonresonant inverse magnetic bremsstrahlung.
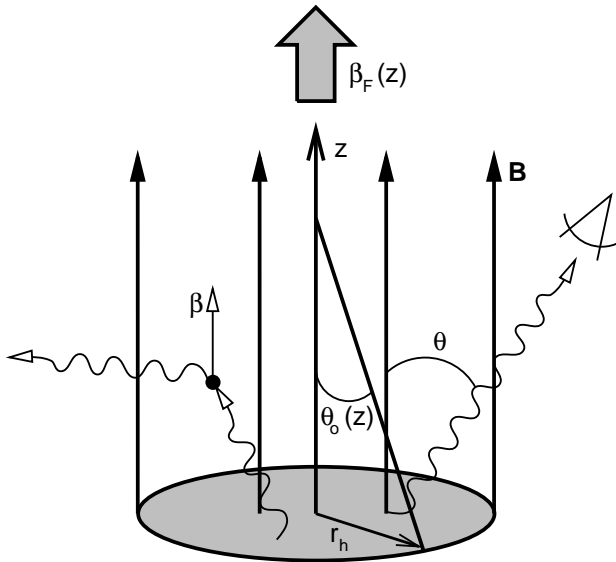
3. PHYSICS OF THE LINE-FORMING REGION

In this section we describe the basic physics that govern the properties of cyclotron lines formed in outflows: the characteristic time scales (§ 3.1), the one-dimensional electron momenta distribution $f(p)$ (§ 3.2), the plasma density profile $n_e(z)$ (§ 3.3), the scattering kinematics (§ 3.4), the scattering profile $\phi(E, \mu, z)$ (§ 3.5), and the gravitational redshift (§ 3.6). We discuss the electron velocity profile $\beta_F(z)$ separately, in § 4.

3.1. *Characteristic Timescales*

Five timescales characterize the physics of the line-forming region: the radiative lifetime $t_{\rm rad}$, the electron-photon relaxation timescale $t_{e\gamma}$, the electron-proton and proton-proton relaxation timescales t_{ep} and t_{pp}, and the particle escape time $t_{\rm esc}$. For simplicity, we estimate the first four timescales for a *static* $[\gamma_F \equiv (1 - \beta_F^2)^{-1/2} = 1]$ line-forming region. This approximation is suitable near the stellar surface, where $\gamma_F < 1.2$. All these timescales are short compared with the burst duration ~ 1–10 s.

The radiative lifetime of an electron in the nth Landau level is just

$$t_{\rm rad} = \frac{\hbar}{\Gamma_n} = 3 \times 10^{-16} \text{ s } n^{-1} B_{12}^{-2} \,, \tag{8}$$

where

$$\Gamma_n = \frac{4n\alpha E_B^2}{3m_e c^2} = 2.6 \times 10^{-3} \text{ keV } nB_{12}^2 \tag{9}$$

is the natural line width for the nth harmonic and α is the fine structure constant.

We determine the timescale for the electrons to come to equilibrium with the photons by calculating the Fokker-Planck coefficient,

$$\left\langle \frac{\delta p^2}{\delta t} \right\rangle_{e\gamma} = \int dE \int \frac{d\Omega}{2\pi} n_x(E, \Omega) \int d\Omega_s \frac{d\sigma}{d\Omega_s} c\delta p^2 \,, \tag{10}$$

where

$$\delta p \approx (\mu - \mu_s)E \tag{11}$$

is the change in momentum during a scattering, the subscript s denotes parameters of the scattered photon, and

$$n_x(E, \Omega, z)dE \frac{d\Omega}{2\pi} = Q(\mu, z)n_x(E, z)dE \frac{d\Omega}{2\pi} \tag{12}$$

is the density of X-ray photons at altitude z with energy between E and $E + dE$ and direction between Ω and $\Omega + d\Omega$. Assuming first harmonic scattering dominates the radiation transfer and taking the limit of zero natural line width, the polarization-averaged scattering cross section is, to lowest order in β and b, approximately

$$\frac{d\sigma}{d\Omega_s} \approx \frac{9}{32} \sigma_T \frac{m_e c^2}{\alpha} \delta(E - E_B) \frac{1 + \mu^2}{2} \frac{1 + \mu_s^2}{2} \tag{13}$$

(see § 3.5), where $\sigma_{\rm T} \equiv (8\pi/3)[e^2/(m_e c^2)]^2 = 6.65 \times 10^{-25}$ cm^2 is the Thomson cross section. Substituting equations (11)–(13) into equation (10) yields

$$\left\langle \frac{\delta p^2}{\delta t} \right\rangle_{e\gamma} = \frac{13\pi}{160} \sigma_T \frac{m_e c^3}{\alpha} n_x(E_B) \,. \tag{14}$$

The equilibration timescale is

$$t_{e\gamma} \approx \frac{\delta p^2}{\langle \delta p^2/\delta t \rangle_{e\gamma}} \sim \frac{(E_B/c)^2}{\langle \delta p^2/\delta t \rangle_{e\gamma}} = \frac{160\alpha}{13\pi\sigma_T m_e c^3 n_x(E_B)} \,. \tag{15}$$

If the electron column depth is sufficiently low so that photons scatter at most one time before escaping the line-forming region (the single scattering approximation), then at all z the photon spectrum is approximately the same as the spectrum initially injected at the hot spot. For a power-law spectrum with spectral index s,

$$n_x(E, z) = n_x(E) = \frac{L_x}{\pi r_h^2 c\xi(s)} E^{-s}$$

$$= 6.6 \times 10^{27} \text{ keV cm}^{-3} \frac{L_{x,40}}{r_{h,5}^2 \xi(s)} \left(\frac{E}{1 \text{ keV}} \right)^{-s} \,, \tag{16}$$

where $r_{h,5} \equiv r_h/10^5$ cm, $L_{x,40} \equiv L_x/10^{40}$ ergs s^{-1} is the luminosity of X-ray photons with $E_1 < E < E_2$, and

$$\xi(s) \equiv \int_{E_1}^{E_2} E^{1-s} dE \,. \tag{17}$$

Throughout this paper we use $E_1 = 1$ keV and $E_2 = 1000$ keV. Substituting equations (16) and (17) into equation (15) and choosing $s = 1$ $[\xi(s) \approx 1000 \text{ keV}]$,

$$t_{e\gamma} \sim 5 \times 10^{-15} \text{ s } L_{x,40}^{-1} r_{h,5}^2 B_{12} \,. \tag{18}$$

By similar arguments, the relaxation time for electron-proton scattering is

$$t_{ep} \sim 3 \times 10^{-6} \text{ s } n_{p,17}^{-1} T_k^{3/2} \left(\frac{\ln \Lambda_{ep}}{20} \right)^{-1} \,, \tag{19}$$

where $T_k \equiv k_B T_e/1$ keV, the Coulomb logarithm is $\ln \Lambda_{ep} \approx 16.2 + 2\ln(T_k B_{12}^{-1})$ (Langer 1981), and $n_{p,17} \equiv n_p/10^{17}$ cm^{-3} is the proton number density $(= n_{e,17} \equiv n_e/10^{17}$ cm^{-3} in a pure hydrogen plasma). We choose a characteristic density, 10^{17} cm^{-3}, where the line-forming region is optically thick in the line core but optically thin in the wings (see § 3.5 below, esp. eqs. [41] and [47] and associated discussion). The relaxation time for proton-proton scattering is

$$t_{pp} \sim 2 \times 10^{-7} \text{ s } n_{p,17}^{-1} T_k^{3/2} \left(\frac{\ln \Lambda_{pp}}{20} \right)^{-1} \,, \tag{20}$$

where $\ln \Lambda_{pp} \approx 15.9 + 0.5\ln(T_k n_{p,17}^{-1})$ (Spitzer 1962). Since the electrons are confined to motion along the field lines, they merely exchange momentum when they scatter with each other, with no change to the overall momenta distribution.

Finally, the time required for an electron to escape the region near the surface, where most scatters take place, is

$$t_{\rm esc} \sim \frac{r_h}{c} = 3 \times 10^{-6} \text{ s } r_{h,5} \,. \tag{21}$$

Comparing the timescales reveals a great deal about what physical processes are important in the line-forming region. Since $t_{e\gamma} \ll t_{ep,pp}$, radiation processes dominate collisional processes. The reason for this is clear: the density of electrons is small compared to the density of resonant photons. While the electron number density in the outflow model is 10^{17}–10^{19} cm^{-3}, the density of resonant photons is

$\approx n_x(E_B)E_d^1 = 4 \times 10^{23} \text{ cm}^{-3} L_{x,40} T_k^{1/2} r_{h,5}^{-2}$, where

$$E_d^n \equiv nE_B\sqrt{\frac{2T_e}{m_e c^2}} = 0.73nB_{12}T_k^{1/2} \qquad (22)$$

is the Doppler width associated with the nth harmonic. Since $t_{ep,pp}$ may be $\gtrsim t_{esc}$, the particles may not spend enough time in the line-forming region to reach equilibrium by particle-particle collisions. However, $t_{e\gamma} \ll t_{esc}$, so there is ample time for the electron momenta distribution to reach equilibrium by electron-photon scatterings, as we discuss in more detail in § 3.2.

Since particle-particle collisions are rare, radiative processes determine the population of excited Landau states. As equations (8) and (18) show, for most situations of interest for line formation in gamma-ray bursts the radiative decay time of the excited states is shorter than the mean time between electron-photon scatters. Consequently, the excited states are not radiatively populated. Thus, we assume throughout this work that an electron is in the Landau ground state ($n = 0$) before and after a scattering. Note, however, that this assumption breaks down for low field strengths and high luminosities where $B_{12}^3 L_{x,40}^{-1} \lesssim 0.1$.

The low rate of particle-particle collisions suggests that pure absorption (i.e., nonresonant inverse magnetic bremsstrahlung) is rare. A more careful analysis confirms this. For $E_B \gg k_B T_e$, the absorption probability *per scattering* is the ratio of absorption to scattering cross sections

$$P_a = \left[\frac{\sigma_a}{\sigma_s}\right]_{B \neq 0} \approx \left[\frac{\sigma_a}{\sigma_T}\right]_{B=0} \approx 2\pi\alpha\sqrt{\frac{m_e c^2}{E_B}}\frac{\hbar^3 c^3 n_p}{E_B^3}$$

$$\approx 1.5 \times 10^{-10} n_{p,17} B_{12}^{-7/2} \qquad (23)$$

(Nelson, Salpeter, & Wasserman 1993). If the line wings are optically thin (see § 3.5), a photon in the line core can escape the line-forming region by scattering to the wings. A core-wing transition occurs in $\sim 1/a$ scatters, where

$$a \equiv \frac{\Gamma_1}{2E_d^1} = 1.8 \times 10^{-3} B_{12} T_k^{-1/2} \qquad (24)$$

is the dimensionless natural line width (Wasserman & Salpeter 1980). The total absorption probability for a resonant photon is, therefore, $a^{-1}P_a \sim 10^{-7} n_{p,17} B_{12}^{-9/2} T_k^{1/2}$. Since this probability is $\ll 1$ throughout the current work, we do not include pure absorption in our calculations.

3.2. *Electron Momenta Distribution*

The timescales that govern the relaxation of electrons in a dynamic, galactic corona model are dramatically different from those of a static, galactic disk model where the photon densities are much lower and the electrons do not escape the line-forming region. Consequently, determining the distribution of electron momenta along the field lines in an outflow requires some care. Two questions must be answered: what is the equilibrium distribution? and Are the electrons in equilibrium—i.e., do they possess the equilibrium distribution?

In the frame of reference moving with the flow, the equilibrium distribution is Maxwellian. We demonstrate this by showing that the electrons and photons constitute a canonical ensemble in equilibrium. In this system the electrons compose a subsystem in thermal contact with a heat bath made up of the photons. To constitute a canonical ensemble, the particles must satisfy two requirements. First, the number of particles in the subsystem must be much smaller than the number of particles in the heat bath. Second, the sum of the energies of the system and the heat bath must be constant (see, e.g., Landau & Lifshitz 1980). Since $n_e \ll n_x E_d^1$ and energy is conserved in electron-photon scattering, both of these conditions are satisfied. Thus, the probability that an electron has an energy $(p^2 + m_e^2 c^4)^{1/2}$ is a Maxwell-Boltzmann distribution.

The electrons relax to equilibrium by electron-photon scattering in a time $\sim t_{e\gamma}$. Note that there is no requirement that the *photon* distribution be thermal or that there be significant electron-proton scattering for the electrons to reach equilibrium. Since $t_{e\gamma} \ll t_{esc}$, the electrons in the outflow have an equilibrium distribution, except in the tail of the Maxwellian; the electrons do not remain in the line-forming region long enough to scatter a sufficient number of times to populate the tail. Since the number of electrons in the tail is small, however, they do not have a significant impact on the properties of the emerging radiation. Therefore, in our calculations we assume an equilibrium distribution at all electron momenta.

The electron temperature at equilibrium (i.e., the Compton temperature) T_C is equal to the temperature of the photons $T_\gamma \equiv (dS/dU)^{-1}$, where S and U are the entropy and energy of the photons, respectively. The Compton temperature can be determined microphysically by summing the energy transferred from the radiation to the plasma in each scatter; at the Compton temperature this sum is zero. Using the single scattering approximation, Lamb, Wang, & Wasserman (1990) calculate T_C in the limits b, $\beta \ll 1$ for a static plasma and first harmonic scattering only.

We adapt their model to a dynamic plasma by finding the Compton temperature T_C^f, where the superscript f indicates quantities measured in the frame of reference moving with the flow. We then boost the momenta distribution back to the lab frame. From equation (6), equation (16), and the Lorentz invariance of $E^{-2}n_x$ (see, e.g., Landau & Lifshitz 1975),

$$n_x^f(E^f, \mu^f) = \frac{\eta(\mu^f - \mu_o^f)}{[\gamma_F(1 + \beta_F \mu^f)]^{s+2}E^s} . \qquad (25)$$

Substituting equation (25) into the formula of Lamb, Wang, & Wasserman (1990),

$$k_B T_C^f = \frac{E_B}{10}\frac{\int_{-1}^{+1}(2 + 7\mu^{f2} + 5\mu^{f4})n_x^f(E_B, \mu^f)d\mu^f}{\int_{-1}^{+1}[1 + (2+s)\mu^{f2} + (s-3)\mu^{f4}]n_x^f(E_B, \mu^f)d\mu^f} , \qquad (26)$$

and using equation (7) for the velocity profile gives $k_B T_C^f \approx 0.25E_B$ for all z. We use this value of the Compton temperature throughout the present work. For a Maxwellian distribution with temperature $k_B T^f \ll \gamma_F^{-2} m_e c^2$ in the frame moving with the flow, the *lab* frame distribution is approximately Maxwellian, with the peak at $p = p_F \equiv \gamma_F \beta_F m_e c$ and temperature $T_e = \gamma_F^2 T_e^f$. The approximation is a good one near the peak, but breaks down in the tail. However, as we point out above, the shape of the distribution in the tail does not have a significant impact on properties of the emerging radiation.

Monte Carlo calculations by Lamb, Wang, & Wasserman (1990) and Isenberg, Lamb, & Wang (1998) show that when higher harmonics, multiple scattering, and the geometry of the line-forming region are included, T_C varies

from the analytic value of equation (26) but is always between $0.2E_B$ and $0.7E_B$. For the line energies observed by *Ginga*, the full-width half-maximum of a line formed in an outflow is relatively insensitive to the temperature since the contribution of thermal broadening to the line width is small. This contribution is just the Doppler width $E_d^1 = 3.2$ keV for $B_{12} = 1.7$, $T_k^f = 5.0$, and $\beta_F = 0.5$. By comparison, the broadening of the line due to the variation in the field with altitude is $\Delta E_B \equiv |dE_B/dz|r_h = 6.0$ keV for the same field strength. Therefore the total line width is $\approx [(\Delta E_B)^2 + (E_d^1)^2]^{1/2} = 6.8$ keV $\approx \Delta E_B$. We show in § 3.5 that the optical depth, and therefore the *equivalent* width, is also insensitive to the temperature. Therefore, equation (26) is sufficiently accurate for determining the properties of the emerging spectrum.

3.3. *Plasma Density Profile*

Conservation of matter in an outflow requires that in the absence of plasma sources or sinks, $n_e(z)\beta_F(z)\tilde{r}^2(z)$ is a constant. The conservation of magnetic flux determines the radius of the outflow $r(z)$, according to equation (5). Therefore, if the plasma at the surface has density n_{eo}, the density at altitude z is (Miller et al. 1991)

$$n_e(z) = n_{eo}\, \frac{\beta_{Fo}}{\beta_F(z)}\, \frac{B(z)}{B_o}\,. \qquad (27)$$

3.4. *Scattering Kinematics*

A resonant scatter may be thought of as an absorption of a photon by an electron, which excites the electron to a higher Landau level, followed by the emission of one or more photons. The absorption conserves energy and momentum along the magnetic field; the portion of the photon's momentum perpendicular to the field that is not transferred to the electron is absorbed by the field. Combining the conservation laws for a transition from the 0 to nth Landau state, and ignoring the finite natural line width, yield the resonant condition ($c = m_e = 1$ throughout this section)

$$1 + E^r - \sqrt{1 + 2nb + \mu^{r2}E^{r2}} = 0\,, \qquad (28)$$

where the superscript r indicates quantities measured in the frame of reference where the electron is at rest prior to scattering. Solving equation (28) for the rest frame resonant photon energy yields

$$E_n^r = \frac{2nb}{1 + \sqrt{1 + 2nb(1 - \mu^{r2})}}\,. \qquad (29)$$

Transforming to the lab frame (the frame of reference where the magnetic dipole is at rest),

$$E_n = \frac{E_n^r}{\gamma(1 - \beta\mu)}\,. \qquad (30)$$

We plot the first harmonic lab frame resonant energy as a function of electron momentum p in Figure 2. As the figure shows, for a given photon energy and $|\mu| < 1$ there are two roots for the electron momentum; p_- and p_+ denote the lower and upper roots, respectively. Physical solutions to the resonant condition do not exist above the cutoff energy

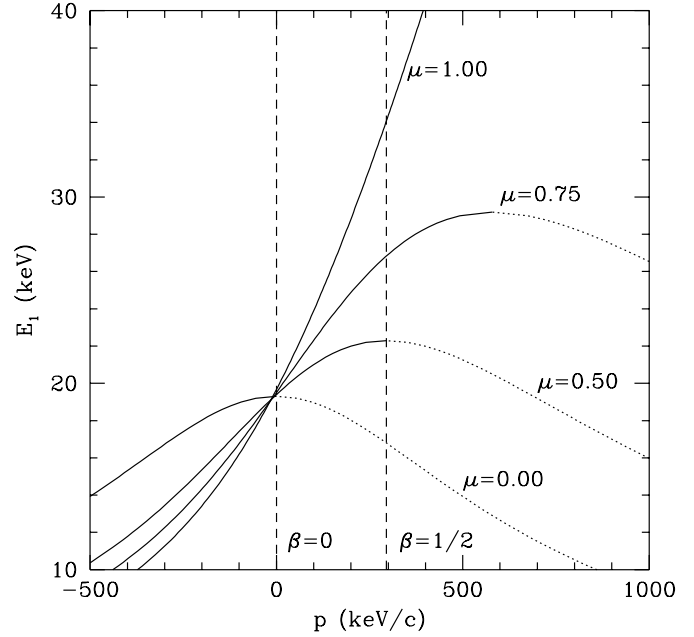$$E_c = \frac{\sqrt{1 + 2nb} - 1}{\sqrt{1 - \mu^2}} \qquad (31)$$

FIG. 2.—First harmonic resonant photon energy E_1 as a function of electron momentum p for $B_{12} = 1.7$ and several photon orientations μ. For a given μ and E_1, the resonant condition has two roots: p_- (*solid lines*) and p_+ (*dotted lines*). Note the cutoff energy E_c, where $p_- = p_+$ and $\beta = \mu$ (i.e., $\mu^r = 0$). Physical roots do not exist for $E > E_c$. The values of p corresponding to $\beta = 0$ and $\beta = 0.5$ are indicated by *dashed lines*.

(Daugherty & Ventura 1978; Harding & Daugherty 1991; Wang, Wasserman, & Lamb 1993). To understand the physical origin of the two momentum roots and the cutoff energy, consider a frame of reference (indicated with a prime) that is moving with a velocity $\beta = \mu$ with respect to the lab frame. In the primed frame, the photon is moving perpendicular to the magnetic field ($\mu' = 0$), since

$$\mu' = \frac{\mu - \beta}{1 - \mu\beta}\,. \qquad (32)$$

In this frame the resonant condition is symmetric with respect to reflection in the plane perpendicular to the field. Thus there must be two equal and opposite solutions for p'; i.e., the E_n' versus p' curve is symmetric about $p' = 0$ and $p_+' = -p_-'$, as shown in Figure 2. For nonzero electron momentum, the photon appears redshifted in the electron rest frame. But at $p' = 0$, $\mu^r = \mu' = 0$, there is no redshift, and the resonant energy has its maximum value, $E_n' = E_c' = E_n^r = \sqrt{1 + 2nb} - 1$. Boosting $p_\pm'$ and E_c' back to the lab frame gives the momentum roots and cutoff energy when $\mu \neq 0$.

Figure 2 illustrates that the scattering kinematics in an outflow are noticeably different from those in a static plasma. For a given μ the line center energy E_{ctr} is equal to the resonant energy corresponding to $\beta = \beta_F$. In a static plasma ($\beta_F = 0$), $E_{\mathrm{ctr}} \approx E_B$ for all μ. The cutoff energy gives the scattering cross section a strong asymmetry near $\mu = 0$ (Lamb et al. 1989) but plays little role at larger μ where the cutoff energy is far above the line center. At these angles, the p_- root dominates the scattering. However in an outflow with, for example, $\beta_F = 1/2$, there is a large variation in the line center energy with photon direction, as expected from equation (30). The effects of the cutoff energy are the most

dramatic at $\mu = \beta_F$, where $E_{ctr} = E_c$. p_- dominates the scattering at larger values of μ while p_+ is dominant at smaller ones.

3.5. Scattering Profile

In calculating the scattering profiles we assume that the vacuum contribution to the dielectric tensor is much larger than the plasma contribution. This is true provided

$$\frac{w}{\delta} = 4 \times 10^{-5} n_{e,17} B_{12}^{-4} \ll \left| 1 - \left(\frac{E_B}{E} \right)^2 \right| , \qquad (33)$$

where $w \equiv (\hbar \omega_p / E_B)^2$ is the plasma frequency parameter, ω_p is the plasma frequency, and δ is the magnetic vacuum polarization parameter (see Adler 1971; Wang, Wasserman, & Salpeter 1988). For the fields and densities considered in the present work, equation (33) breaks down above $z \sim R_*$, where the field strength becomes small. However, the condition is satisfied near the stellar surface, where most of the scattering takes place. This condition also breaks down very near the line center, where $E \approx E_B$. However, the effect on the emerging spectrum is negligible since the line properties are determined primarily by the scattering profile in the line wings (see below).

The scattering cross sections we use are valid in the limit

$$\left(\frac{E^r}{m_e c^2} \right)^2 \frac{1}{b} \ll 1 , \qquad (34)$$

which holds throughout the present work. In this limit the scattering cross section approaches the classical magnetic Compton cross section. When evaluated in the prescattered electron's rest frame and averaged over the azimuthal angle (appropriate for azimuthally symmetric line-forming regions such as those studied here) this cross section is given by (Canuto, Lodenquai, & Ruderman 1971; Herold 1979; Ventura 1979; Wasserman & Salpeter 1980; Wang et al. 1988; Lamb et al. 1990; Harding & Daugherty 1991; Graziani 1993; Isenberg et al. 1998):

$$\frac{d\sigma^r}{d\Omega_s^r} = \frac{d\sigma_0^r}{d\Omega_s^r} + \frac{d\sigma_1^r}{d\Omega_s^r} . \qquad (35)$$

The first term on the right is the continuum part of the cross section

$$\frac{d\sigma_0^r}{d\Omega_s^r} = \frac{3}{16\pi} \sigma_T$$

$$\times \begin{cases} 2 \sin^2 \theta^r \sin^2 \theta_s^r + \left(\dfrac{E^r}{E^r + E_B} \right)^2 \mu^{r2} \mu_s^{r2} & (\| \to \|) \\[2ex] \left(\dfrac{E^r}{E^r + E_B} \right)^2 \mu^{r2} & (\| \to \perp) \\[2ex] \left(\dfrac{E^r}{E^r + E_B} \right)^2 \mu_s^{r2} & (\perp \to \|) \\[2ex] \left(\dfrac{E^r}{E^r + E_B} \right)^2 & (\perp \to \perp) \end{cases} . \qquad (36)$$

The symbols at the right of equation (36) indicate the polarization mode, parallel or perpendicular, of the initial and scattered photon. The resonant part of the cross section is

$$\frac{d\sigma_1^r}{d\Omega_s^r} = \frac{9}{64} \frac{\sigma_T m_e c^2}{\alpha} \left[\frac{4E^{r3}}{E_B (E^r + E_B)^2} \right]$$

$$\times \frac{\Gamma_1 / 2\pi}{(E^r - E_1^r)^2 + (\Gamma_1/2)^2} \times \begin{cases} \mu^{r2} \mu_s^{r2} & (\| \to \|) \\ \mu^{r2} & (\| \to \perp) \\ \mu_s^{r2} & (\perp \to \|) \\ 1 & (\perp \to \perp) \end{cases} . \qquad (37)$$

The corresponding polarization-averaged cross sections are calculated by summing equations (36) and (37) over the final polarization states and averaging over the initial.

The contribution of $n > 1$ harmonic scattering to the scattering profile can be calculated approximately by treating higher harmonic scattering as the absorption of a photon followed by the emission of one or more photons. Then the total rest frame cross section

$$\sigma^r \approx \sum_{n=0}^{\infty} \sigma_n^r , \qquad (38)$$

where

$$\sigma_0^r = \sum_{\|, \perp} \int d\Omega_s^r \frac{d\sigma_0^r}{d\Omega_s^r} , \quad \sigma_1^r = \sum_{\|, \perp} \int d\Omega_s^r \frac{d\sigma_1^r}{d\Omega_s^r} \qquad (39)$$

(the sums are over the *final* polarization states), and

$$\sigma_{n>1}^r = \frac{3}{4} \frac{\pi m_e c^2 \sigma_T}{\alpha} b^{n-1} \frac{(n^2/2)^{n-1}}{(n-1)!}$$

$$\times \frac{\Gamma_n / 2\pi}{(E^r - E_n^r)^2 + (\Gamma_n/2)^2} (1 - \mu^{r2})^{n-1} \times \begin{cases} \mu^{r2} & (\|) \\ 1 & (\perp) \end{cases} \qquad (40)$$

is the total cross section for absorption at the nth harmonic (Daugherty & Ventura 1977; Fenimore et al. 1988). The approximation (38) is valid provided the line-forming region is not optically thick in the line wings of the first harmonic (see below; see also Wasserman & Salpeter 1980; Lamb et al. 1989; Isenberg et al. 1998), i.e.,

$$\tau_1 \lesssim 1/a , \qquad (41)$$

where τ_1 is the polarization and frequency-averaged first harmonic optical depth for photons moving parallel to the magnetic field (see below), and a is given by equation (24). Equation (41) holds for all cases we study in the present work.

From the Lorentz invariance of the optical depth (see, e.g., Rybicki & Lightman 1979), the lab frame cross section σ_n is related to σ_n^r by

$$\sigma_n = (1 - \beta\mu) \sigma_n^r . \qquad (42)$$

We average the lab frame cross sections over the electron momenta distribution and divide by the Thomson cross section to obtain the scattering profile for the nth harmonic

$$\phi_n(E, \Omega) \equiv \frac{1}{\sigma_T} \int dp f(p) \sigma_n . \qquad (43)$$

The line can be divided into the line core ($|x_n/\mu| \ll 1$) and the line wings ($|x_n/\mu| \gg 1$), where $x_n \equiv (E - E_n)/E_d^n$ is the dimensionless frequency shift (Wasserman & Salpeter 1980). In the line core, the electron distribution dominates the profile so that $\phi_n \propto f(x_n^2/|\mu|)$. In the wings, the tail of the Lorentzian distribution dominates so that $\phi_n \propto a x_n^{-2}$. We

refer to the wing at energies below the line center as the red wing and the wing at energies above the line center as the blue wing. Wasserman & Salpeter (1980) show that for the first harmonic, the core-wing boundary appears at $|x_1/\mu| \approx 2.62 - 0.19 \ln{(100a/\mu)}$.

The optical depth at the nth harmonic is equal to

$$\tau_n(E, \mu) = \sigma_T \int \phi_n(E, \mu) \frac{n_e(z)dz}{|\mu|} . \tag{44}$$

The first harmonic optical depth along the line of sight with the shortest escape path characterizes the radiation transfer. In the outflow model this line of sight is along the field, because of the change in the cyclotron energy with altitude: a photon can escape the line core by diffusing to an altitude where it is in the wings. If the characteristic distance a photon climbs before escaping the line core

$$\Delta z_{\rm esc} \equiv \left| \frac{E_d^1}{dE_B/dz} \right|_{z=0} \ll R_* , \tag{45}$$

then the energy-averaged first harmonic optical depth along the field is

$$\tau_1 \approx \sigma_T \left| \int \phi_n(E, 1) \frac{dE}{E_d^1} \right|_{z=0} n_{eo} \Delta z_{\rm esc} . \tag{46}$$

Averaging over the photon polarization and adopting the velocity profile from the model of MT and a Gaussian electron momentum distribution yields

$$\tau_1 \approx 82 \frac{n_{eo,17} r_{h,5}}{B_{o,12}(1 - 4.5r_h/R_*)} . \tag{47}$$

For $r_h/R_* = 0.1$, equation (47) gives $\tau_1 \approx 149 n_{eo,17} r_{h,5} B_{o,12}^{-1}$, and the condition equation (41) implies $n_{eo,17} \lesssim 4 r_{h,5}^{-1} T_k^{1/2}$. Comparing equation (47) for τ_1 to the corresponding optical depth for a static slab line-forming region is instructive. In a slab with a uniform magnetic field parallel to the slab normal, the optical depth along the field is $\tau_1 = 1500 N_{e,22} B_{12}^{-1} T_k^{-1/2}$ (Lamb et al. 1990), where $N_{e,22}$ is the column depth in units of 10^{22} cm^{-2}. The optical depth of an outflow is about an order of magnitude smaller than that of a slab with a comparable column depth, i.e., a slab whose column depth is equal to the *radial* column depth $n_{eo} r_h$ of the outflow. The optical depth is smaller for the outflow because the distance a photon needs to travel to escape the line core is smaller than r_h; it can escape by climbing to an altitude where the cyclotron energy is less than the photon energy by more than a Doppler width. Note that in the outflow, the optical depth is independent of the electron temperature, in contrast to the slab where $\tau_1 \sim T_k^{-1/2}$. The reason for this is that in the outflow the decrease in $d\tau_1/dz$ with increasing temperature is offset by the greater distance a photon needs to climb to escape the line core.

3.6. Gravitational Redshift

A photon that travels from the stellar surface ($z = 0$) to an observer at $z = \infty$ experiences a gravitational redshift

$$\frac{E(0) - E(\infty)}{E(0)} = \frac{GM_*}{c^2 R_*} = 0.2 \left(\frac{M_*}{M_{ch}} \right) \left(\frac{R_*}{10^6 \text{ cm}} \right)^{-1} , \tag{48}$$

where M_* is the stellar mass and $M_{ch} = 2.8 \times 10^{33}$ g is the Chandrasekhar mass. Because the redshift changes the photon energy by only $\approx 20\%$, we do not include it in our calculations. The redshift reduces the cyclotron line width as well as the energy of individual photons, so the redshift narrows the lines. Since we wish to determine whether narrow lines can be formed in an outflow, ignoring the redshift is a *conservative* assumption.

4. ELECTRON VELOCITY PROFILES

The net force on a particle in an outflow is the sum of the radiation and gravitational forces, $F = F_{\rm rad} + F_g$. For the luminosities appropriate for a gamma-ray burst in the galactic corona, the radiation force is much larger than the gravitational force, so that $F \approx F_{\rm rad}$. Since the electrons are restricted to motion along the field lines, only the component of the radiation force parallel to the magnetic field is of interest. In § 4.1 we use the approximate, analytic model of MT to calculate the radiation force along the field line. We then integrate the equations of motion to determine the velocity profile. In § 4.2 we use a Monte Carlo radiative transfer code to determine the velocity profile self-consistently.

4.1. Analytic Model of Mitrofanov & Tsygan

MT calculate the radiation force in an outflow using a single scattering approximation. They show that when first harmonic scattering dominates the radiation transfer, and $\Gamma_r \to 0$, the component of the radiation force along the field line is

$$F_{\rm rad} = \pi^2 \sigma_T \frac{E_B^2}{\Gamma_r} E_B \int (\mu - \beta) \left[1 + \left(\frac{\mu - \beta}{1 - \beta\mu} \right)^2 \right.$$
$$\left. + P_l \frac{1 - \mu^2}{\gamma^2(1 - \beta\mu)^2} \right] \times \frac{1}{1 - \beta\mu} n_x \left[\frac{E_B}{\gamma(1 - \beta\mu)}, \mu \right] d\mu , \tag{49}$$

where P_l is the degree of linear polarization, i.e., the fraction of perpendicular-mode photons minus the fraction of parallel-mode photons. Because equation (49) is linear in the scattering cross section, the radiation force for the polarization-averaged cross section is the same as the radiation force for polarized cross sections with $P_l = 0$. Substituting the power-law photon spectrum we use in the present work (eqs. [12] and [16]) into the radiation force gives

$$F_{\rm rad} = \frac{\pi \sigma_T}{c} \frac{E_B^2}{\Gamma_r} \frac{L_x \gamma^s E_B^{1-s}}{r_h^2 \xi(s)} I_1 , \tag{50}$$

where

$$I_1 \equiv \int_{\mu_o}^1 (\mu - \beta) \left[1 + \left(\frac{\mu - \beta}{1 - \beta\mu} \right)^2 + P_l \frac{1 - \mu^2}{\gamma^2(1 - \beta\mu)^2} \right]$$
$$\times (1 - \beta\mu)^{s-1} Q(\mu) d\mu . \tag{51}$$

Equation (50) is equivalent to

$$\frac{d\gamma}{d\tilde{z}} = r_h \begin{Bmatrix} (m_p c^2)^{-1} \\ (m_e c^2)^{-1} \end{Bmatrix} F_{\rm rad}$$
$$= \begin{Bmatrix} 2.4 \times 10^5 \\ 4.5 \times 10^8 \end{Bmatrix} L_{x,40} \gamma^s \left(\frac{E_B}{1 \text{ keV}} \right)^{1-s}$$
$$\times r_{h,5}^{-1} \left[\frac{\xi(s)}{1000 \text{ keV}^{2-s}} \right]^{-1} I_1 , \tag{52}$$

where the upper expressions in curly brackets are for an electron-proton plasma and the lower expressions are for an electron-positron plasma.

By integrating equation (52), we calculate the velocity as a function of altitude for an electron in an electron-proton plasma, injected at the origin with $\beta = 0$. We use a $1/E$ photon spectrum with $P_l = 0$. We plot the result in Figure 3. The curve shows three distinct regimes, which MT call free acceleration, kinematic restriction, and energetic restriction. At any altitude z there exists a velocity $\beta_{(F=0)}$ where the radiation force is equal to zero. Near the surface, $\beta_{(F=0)} \approx 0.5$, which corresponds to $\gamma_{(F=0)} \approx 1.15$. In the free acceleration regime $\beta < \beta_{(F=0)}$ and the electron accelerates rapidly.

When β reaches $\beta_{(F=0)}$ the electron enters the regime of kinematic restriction. The distance it travels before reaching this regime is

$$\tilde{z}_{KR} \sim \frac{\Delta\gamma}{d\gamma/d\tilde{z}} \sim \begin{Bmatrix} 10^{-6} \\ 10^{-9} \end{Bmatrix} L_{x,40}^{-1} \left(\frac{E_B}{1 \text{ keV}} \right)^{s-1}$$

$$\times r_{h,5} \left[\frac{\xi(s)}{1000 \text{ keV}^{2-s}} \right]. \quad (53)$$

In the kinematic restriction $\beta \approx \beta_{(F=0)}$. The electron requires a small radiation force to overcome the force of gravity and keep pace with the increase of $\beta_{(F=0)}$ with altitude. However the difference between the actual velocity and the zero force velocity is approximately one part in 10^6.

As the electron continues to climb, the radiation becomes more diffuse and eventually carries too little energy to maintain the particle at the zero force velocity; i.e.,

$$\frac{d\gamma_{(F=0)}}{d\tilde{z}} > \frac{d\gamma}{d\tilde{z}}. \quad (54)$$

The particle enters the energetic restriction regime and the Lorentz factor levels off to $\gamma = \gamma_{\max}$. For $z \gg 1$ and

$s = 1$, equation (51) becomes

$$I_1 \approx \frac{1}{2\tilde{z}^2} \left(\frac{1}{\gamma^2} - \frac{3}{2\tilde{z}^2} \right) \leq \frac{1}{2\tilde{z}^2 \gamma^2}, \quad (55)$$

so $\gamma_{(F=0)} \approx (2/3)^{1/2}\tilde{z}$. Substituting $\gamma \sim \tilde{z}$ and equation (55) into equation (54), the energetic restriction begins at

$$\tilde{z}_{ER} \sim \gamma_{\max} \sim \begin{Bmatrix} 100 \\ 1000 \end{Bmatrix} L_{x,40}^{1/3} r_{h,5}^{-1/3}. \quad (56)$$

We caution that the discussion of the energetic restriction is highly speculative. Since the cyclotron energy in this regime is below burst detector thresholds, we do not know the relevant part of the photon spectrum observationally.

Figure 3 and equations (53) and (56) clearly show that the electron is in the kinematic restriction throughout the region of interest for line formation, except for about a millimeter of free acceleration near the surface. Consequently, we assume $F_{\rm rad} = 0$ for the remainder of the present work.

Equation (52) gives the acceleration of an *individual* electron. For a group of electrons whose velocities are distributed thermally about the flow velocity, the radiation force should be averaged over the velocity distribution. Setting the average force to zero and solving for the flow velocity yields a velocity almost indistinguishable from the zero force velocity of an individual electron, i.e., $\beta_F \approx \beta_{(F=0)}$. There are two reasons for this. First, the corrections to the velocity due to temperature are $\sim k_B T_e/m_e c^2 \ll \beta_{(F=0)}$. Second, the Maxwell-Boltzmann distribution is symmetric, so the corrections due to electrons with velocities on each side of the bulk flow velocity tend to cancel.

Figure 4 shows the zero force velocity profile given by equation (50) with $P_l = 0$ and $s = 0.5$, 1.0, and 2.0. For comparison, we also plot the approximate velocity profile of
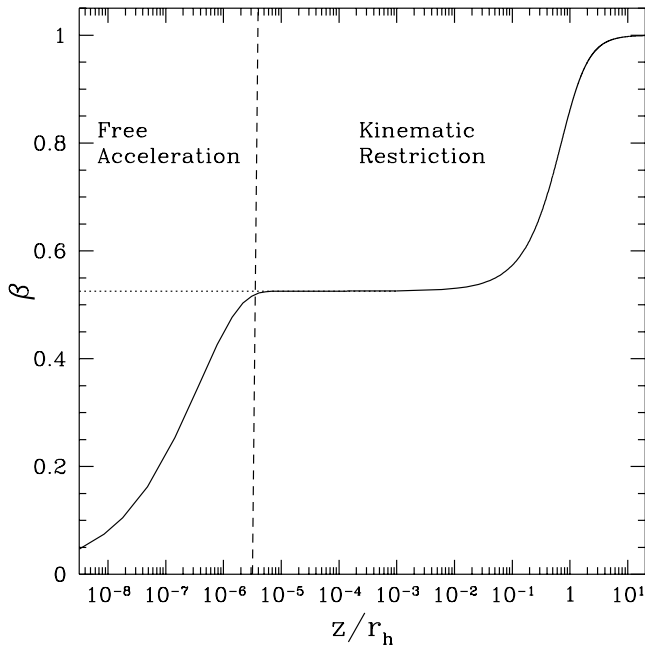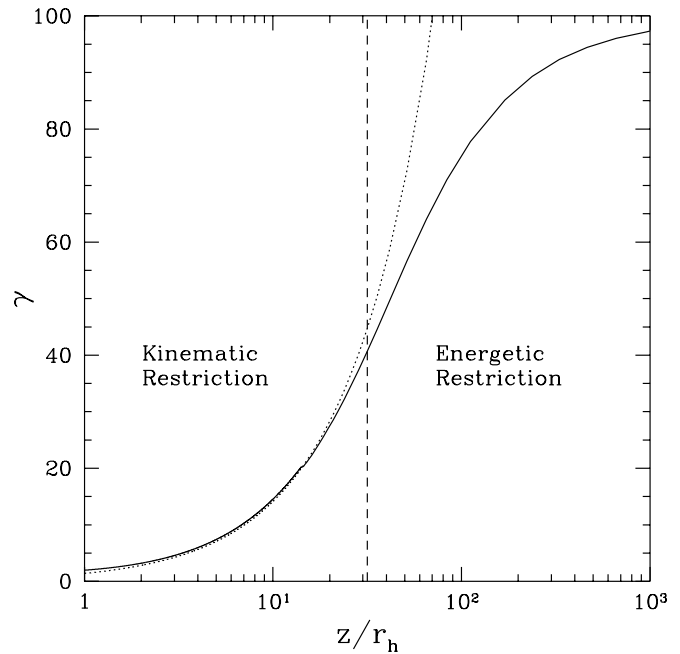

FIG. 3a

FIG. 3b

FIG. 3.—Radiation-driven acceleration of an electron-proton pair in a strong magnetic field, according to the model of Mitrofanov & Tsygan (1982). The particles are injected at the origin of a hot spot with radius r_h. Radiation with a $1/E$ spectrum and X-ray luminosity $L_x = 10^{40}$ ergs s^{-1} is injected semi-isotropically and uniformly across the hot spot. (a) Velocity β as a function of altitude $\tilde{z}$. (b) Lorentz factor γ. The *solid lines* are the β and γ of a pair with zero initial velocity. The *dotted lines* indicate the values of β and γ where the radiation force $F_{\rm rad} = 0$.
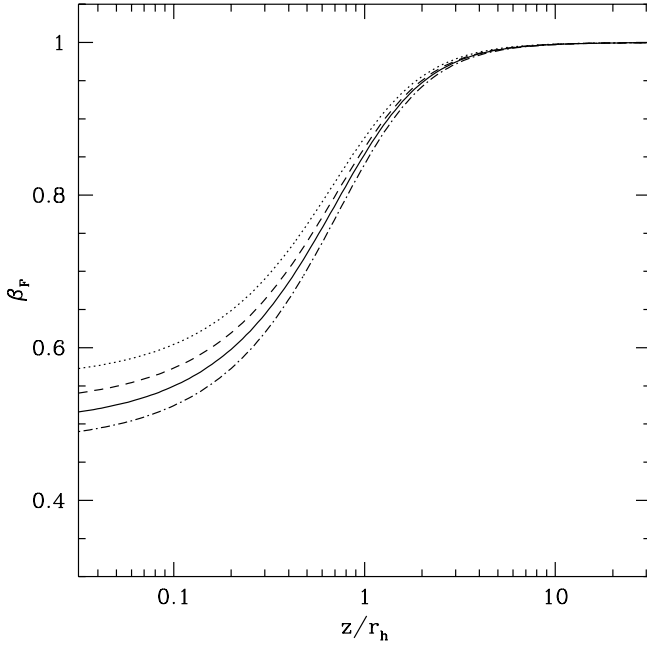
FIG. 4.—Effect of the spectral index s on the velocity profile. Flow velocity as a function of altitude calculated from the model of Mitrofanov & Tsygan (1982) for $s = 0.5$ (*dotted line*), 1.0 (*dashed line*), and 2.0 (*dot-dashed line*) and unpolarized scattering. The approximate profile $\beta_F = 0.5(1 + \mu_o)$ is shown for comparison (*solid line*).
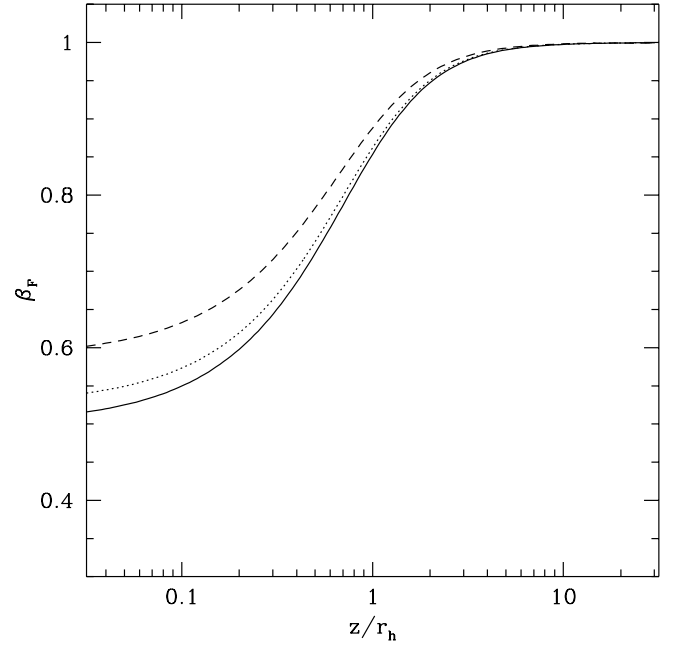
FIG. 5.—Effect of the photon polarization on the velocity profile. Flow velocity as a function of altitude calculated from the model of Mitrofanov & Tsygan (1982) for spectral index $s = 1$ and polarized scattering. The fraction of injected photons in parallel mode is $P_l = -1.0$ (*dashed line*), 0.0 (*dotted line*), and 1.0 (*solid line*).

equation (7). For $s < \approx 1.5$, the flow velocity is larger than the approximate value. This is due to the $1 + \mu^2$ dependence of the scattering cross section, which the approximate calculation does not take into account. Photons moving at large μ, which carry more momentum along the field line, are more likely to scatter, increasing the radiation force and hence the flow velocity. As the spectral index increases, there are fewer photons with large energies. Consequently $F_{\rm rad}$ is smaller and β_F decreases.

Figure 5 shows the velocity profile for $s = 1$ and $P_l = -1$, 0, and 1. In perpendicular mode, the scattering cross section is independent of μ and the velocity profile is the same as the approximate one. As the fraction of parallel-mode photons increases, photons at small angles to the field are more likely to scatter and the flow velocity increases.

4.2. Self-consistent Monte Carlo Calculation

We calculate self-consistent velocity profiles by iterating calculations of the radiation transfer and the hydrodynamics. The procedure is conceptually similar to the one Wang & Frank (1981) use to determine the velocity profile and radiation energy density in the accretion column of an accretion-powered pulsar. For the radiation transfer, we have adapted a Monte Carlo code written for static, slab line-forming regions (see Wang et al. 1988; Wang et al. 1989; Isenberg et al. 1998) to the geometry and physical conditions in an outflow. The code calculates the radiation force, which we integrate to determine the velocity profile for the next iteration. We repeat the process until the radiation force is zero everywhere, within the statistical uncertainty of the Monte Carlo code.

In addition to the physical processes included in the analytic model of MT, the Monte Carlo calculation permits multiple scattering, higher harmonics, and a finite natural line width. The analytic model assumes a disk photon source with electrons on the cylinder axis or, equivalently, a point photon source with electrons anywhere in the outflow. The Monte Carlo code permits electrons anywhere in the outflow and either a point or a disk photon source.

Figure 6 illustrates the effect of these enhancements on the velocity profile. The figure shows the velocity profile for a $1/E$ photon spectrum injected into a line-forming region with $r_h = 0.1 R_*$, $B_{o,12} = 1.7$, and $n_{eo} = 10^{17}$ cm^{-3}. We use polarization-averaged cross sections in all simulations, except where otherwise indicated. As the figure shows, for a Monte Carlo calculation with first harmonic scattering only, a point photon source, and $\Gamma_r = 0$, the self-consistent velocity profile is very similar to the profile calculated from MT's analytic model. The two calculations agree within about 10% at the stellar surface. To understand the difference, consider the optical depth of a region which is small enough that the magnetic field and flow velocity do not change significantly. The fraction of photons with energy E and orientation μ which scatter in this region is $f_s \approx 1 - \exp\left[-\tau(E, \mu)\right]$. Assuming that first harmonic scattering dominates the radiation transfer, expanding in τ, and averaging over energy yields, in the frame of reference moving with the flow,

$$f_s^f \approx 1 - e^{-3/4\tau_1(1 + \mu'^2)}$$

$$= \tfrac{3}{4}\tau_1(1 + \mu'^2)[1 - \tfrac{3}{8}\tau_1(1 + \mu'^2) + O(\tau_1^2)] , \quad (57)$$

where τ_1 is the energy *and angle* averaged optical depth. When the optical depth is very small ($\tau_1 \ll 1$), f_s is proportional to the cross section, consistent with the single scattering approximation used by MT. Since $F_{\rm rad} \propto \tau_1$, and $F_{\rm rad} = 0$ at the flow velocity, the velocity profile is not sensitive to τ_1 at very small optical depths. However, as the optical depth increases, the higher order terms in equation (57) become significant. Consequently, photons traveling at
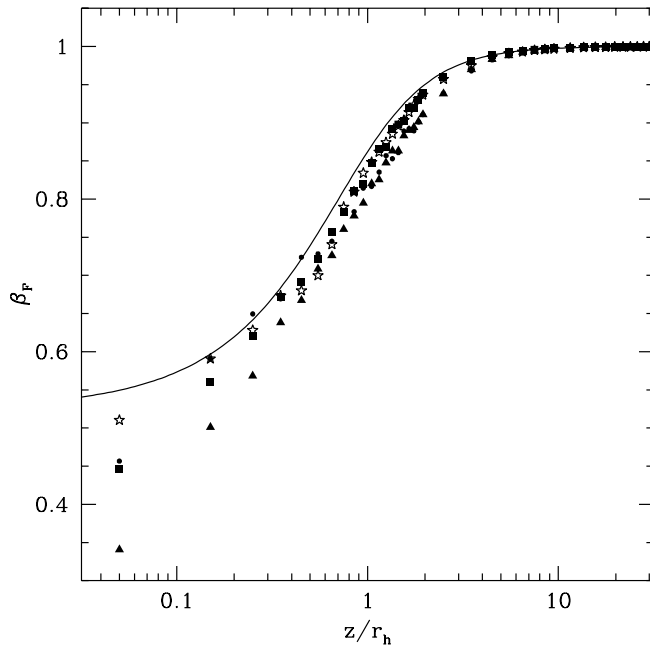
FIG. 6.—Self-consistent Monte Carlo calculations of velocity profiles for a $1/E$ spectrum injected into a line-forming region with hot spot radius $r_h = 0.1R_*$, dipole field $B_{o,12} = 1.7$, and surface electron density $n_{e,o} = 10^{17}$ cm^{-3}. The profile is shown for first harmonic scattering, point photon source, and natural line width $\Gamma_r = 0$ (stars); first harmonic scattering, point source, and Γ_r = finite (squares); first harmonic scattering, disk source, and Γ_r = finite (dots); and continuum and first three harmonic scattering, disk source, and Γ_r = finite (triangles). The profile calculated from the model of Mitrofanov & Tsygan (1982) is shown for comparison (solid line).
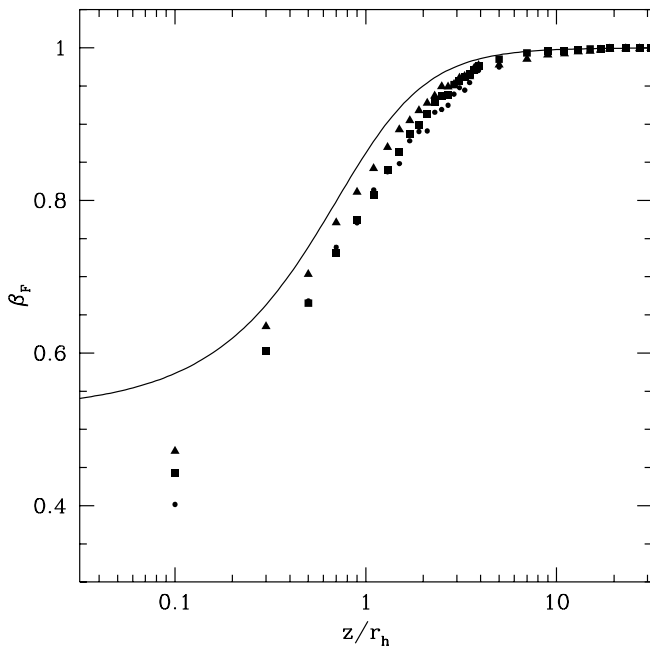
FIG. 7.—Effect of electron density on the velocity. Velocity profiles for a GRB 880205 continuum spectrum injected uniformly across a hot spot with radius $r_h = 0.05R_*$. The line-forming region has dipole field $B_{o,12} = 1.7$, electron temperature $k_B T_e^f = 0.25E_B$, a self-consistent velocity profile, unpolarized continuum and first three harmonic scattering with finite natural line width, and surface electron densities $n_{e,o} = 10^{16}$ cm^{-3} (squares), $n_{e,o} = 10^{17}$ cm^{-3} (dots), and $n_{e,o} = 10^{18}$ cm^{-3} (triangles). The profile calculated from the model of Mitrofanov & Tsygan (1982) is shown for comparison (solid line).

large angles to the field are more likely to scatter, reducing β_F.

The finite natural line width reduces the flow velocity even further. We attribute this to scattering of photons in the line wings. Wing scattering has the greatest impact at $\mu = 0$ where there is no thermal broadening of the cyclotron line. Consequently, the finite natural line width increases the number of scatters of photons at large angles to the magnetic field, decreasing β_F.

When photons are injected semi-isotropically at the origin of the hot spot, the mean distance from the injection point to the walls of the cylinder is $\pi/2r_h \approx 1.57r_h$. When they are injected uniformly across the hot spot, this distance falls slightly, to $4/3r_h \approx 1.33r_h$, resulting in a proportional drop in mean optical depth along the line of sight. Since the dependence of the velocity profile on optical depth is second order and the change in optical depth is small, the method of injection does not have a significant impact on the profile, as Figure 6 shows.

When higher harmonic scattering is added to the calculation, the flow velocity drops further. This is clear from the $(1 - \mu^2)^{n-1}$ dependence of the scattering cross sections. Photons with small μ are more likely to scatter at higher harmonics, lowering the radiation force.

We illustrate the effect of the optical depth on the velocity profile in greater detail in Figure 7. The figure shows velocity profiles for a line-forming region with $r_h = 0.05R_*$ and $B_{o,12} = 1.7$. Continuum and first three harmonic scattering with finite natural line width are included in the calculation. The injected photon spectrum is the best fit of a double power law to the continuum spectrum of GRB 880205, $n_x(E) \propto E^{-s}$, where $s = \alpha_1 = 0.8479$ for $E < E_{\rm break} = 107.8$ keV and $s = \alpha_2 = 1.199$ for $E > E_{\rm break}$ (P. E. Freeman 1993, private communication; see also Fenimore et al. 1988; Wang et al. 1989). As n_{eo} increases from 10^{16} cm^{-3} to 10^{17} cm^{-3}, the flow velocity decreases, as expected from equation (57). However, as the plasma density increases further, to 10^{18} cm^{-3}, the trend reverses. This is because at the larger plasma density there is significant angular redistribution of the photons; equation (57) does not take this redistribution into account. Because of the motion of the plasma, many photons are scattered to large values of μ (see Figs. 8 and 15, below). Further scattering of these photons increases $F_{\rm rad}$ and β_F.

5. MONTE CARLO SPECTRA

Figure 8 shows the emerging photon flux $N(E, \mu)$, in arbitrary units, from a Monte Carlo calculation with first harmonic scattering only and zero natural line width. The injected photon flux $N_i(E, \mu)$ is a power law with $s = 1$. Injection is at the origin of a hot spot with radius $r_h = 0.1R_*$. At the stellar surface the magnetic field strength is $B_{o,12} = 1.7$ and the electron density is $n_{e,o} = 10^{17}$ cm^{-3}. The calculation uses the approximate velocity profile of equation (7). For comparison, we also plot a pure absorption spectrum,

$$N_{\rm abs}(E, \mu) = N_i(E, \mu) \exp\left[-\sum_n \tau_n(E, \mu) \right], \quad (58)$$

where in this case the sum stops at $n = 1$.

The motion of the plasma has a significant impact on the spectrum. The line centers are shifted from their rest frame values $E \approx nE_B$, according to equation (30). In addition, the
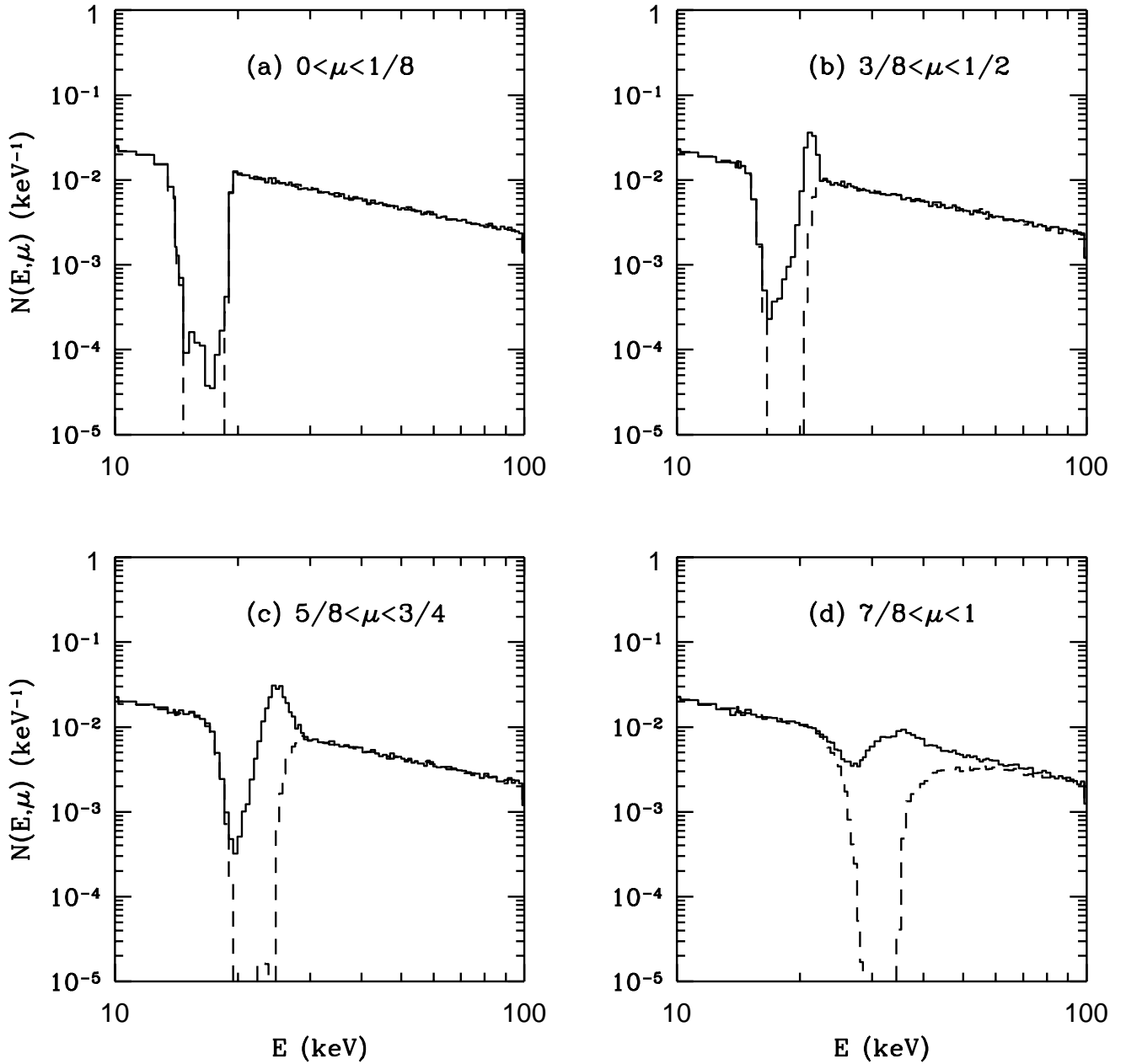
Fig. 8.—Monte Carlo emerging photon number spectra for several viewing angles for a $1/E$ continuum spectrum injected at the origin of a hot spot with radius $r_h = 0.1R_*$. The line-forming region has a dipole field $B_{o,12} = 1.7$, electron temperature $k_B T_e^f = 0.25E_B$, surface electron density $n_{e,o} = 10^{17}$ cm^{-3}, velocity profile $\beta_F = 0.5(1 + \mu_o)$, and unpolarized first harmonic scattering with zero natural line width (solid lines). Pure absorption spectra (dashed lines) are shown for comparison.

high plasma velocity beams scattered photons along the magnetic field. Consequently, when viewed perpendicular to the field (panel a), the scattered spectrum is nearly identical to the absorption spectrum, since photons absorbed at large angles to the field are reemitted at smaller ones. As μ approaches $\beta_{Fo} = 1/2$, the cutoff energy E_c is near the line center and plays an important role in determining the properties of the line, as we note in § 3.4. Since E_c falls with altitude, photons with $E < E_c$ can escape the line core by diffusing upward until $E > E_c$. The photons then escape the line-forming region without further scattering. The escape of photons in the blue wing is responsible for the spike in panel b. This feature becomes broader with increasing μ, because of the enhanced Doppler broadening of the line when viewed along the field and because of the large

number of scattered photons that emerge at high μ. As μ approaches unity, the line is almost entirely filled in by scattered photons, forming a broad emission-like feature.

The features in Figure 8 are narrow. The equivalent width of the line in panel a is $W_{E1} = 5.3$ keV, which is comparable to the first harmonic line width in the Ginga observations of GRB 880205, $W_{E1} = 3.7$ keV. The reason the line is so narrow, in spite of the variation of the magnetic field with altitude, is that the vast majority of scatters occurs in a region close to the surface where the variation of the field is small. We illustrate this in Figure 9, which shows the number of scatters as a function of altitude dN_s/dz, in arbitrary units. We plot dN_s/dz for the simulation in Figure 8, as well as for simulations with first three harmonic and continuum scattering and both $\beta_F = 0.5(1 + \mu_o)$ and a self-
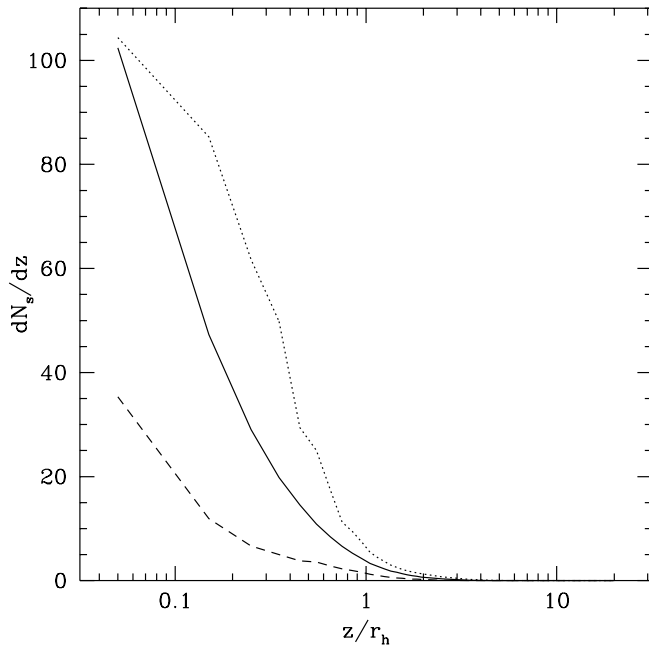
FIG. 9.—Number of scatters per photon per unit distance dN_s/dz, in arbitrary units, as a function of altitude above the stellar surface z/r_h for a $1/E$ continuum spectrum injected into a line-forming region with dipole field $B_{o,12} = 1.7$, electron temperature $k_B T_e^f = 0.25E_B$, surface electron density $n_{e,o} = 10^{17}$ cm^{-3}, and unpolarized scattering. Calculations are shown for continuum and first three harmonic scattering with self-consistent (*solid line*) and $\beta_F = 0.5(1 + \mu_o)$ (*dotted line*) velocity profiles, and first harmonic scattering with a $\beta_F = 0.5(1 + \mu_o)$ (*dashed line*) velocity profile.

consistent velocity profile. Adding the higher harmonics increases the number of scatters. In all cases, few scatters occur above $\tilde{z} = 1$. The decrease in the number of scatters with altitude is due to the escape of photons through the sides of the cylindrical line-forming region. The decrease is analogous to the decrease in the number of *unscattered* photons, described by equation (6).

Figure 10 shows that even though the natural line width is small, it has a noticeable impact on spectra formed in an outflow and needs to be included in radiation transfer calculations. The figure shows the emerging photon flux from simulations with a $1/E$ spectrum injected at the origin of a hot spot with radius $r_h = 0.1R_*$. At the surface the magnetic field strength is $B_{o,12} = 1.7$ and the electron density is $n_{e,o} = 10^{17}$ cm^{-3}. The simulations use self-consistent velocity profiles. When the finite natural line width is included, the scattering profile is no longer zero above E_c. Consequently, photons in the blue wing spike at $\mu \approx \frac{1}{2}$ do not escape the line-forming region immediately. They continue to scatter to larger values of μ, depopulating the spike and filling in the lines at higher μ to a greater extent than when $\Gamma_r = 0$.

When the photons are injected uniformly across the hot spot instead of at the origin, the lines become shallower. This is due to the reduction in the optical depth seen by photons that are injected closer to the edges of the hot spot. We illustrate this in Figure 11 for a line-forming region with the same parameters as Figure 10.

Adding continuum and second and third harmonic scattering to the simulation of Figure 11 yields the spectra shown in Figure 12. For comparison, we also plot the corresponding spectra for first harmonic scattering only and pure

absorption. The higher harmonic features in the scattering spectrum are almost identical to the absorption features. This is because the scattering cross sections favor Raman scattering at the higher harmonics; i.e., most photons absorbed at $n = 2$ and 3 are reemitted as two or three spawned photons at lower harmonics (Bussard & Lamb 1982). Consequently the scattering profiles suffice to explain the properties of the higher harmonic lines. As μ increases the lines become wider as a result of Doppler broadening, but shallower as a result of the $(1 - \mu^{r2})^{n-1}$ dependence of the scattering cross section. The asymmetric shape is characteristic of lines formed in an outflow—as the altitude increases, both the cyclotron energy and the plasma density decrease, resulting in an extended tail in the red wing. This is apparent, for example, in the second harmonic line in panel b. At the first harmonic, the absorption-like features at small μ are shallower and the emission-like features at large μ are more sharply peaked than in the simulations with first harmonic scattering only. This is because additional photons are present at the first harmonic due to spawning. These photons fill in the absorption-like features and build up the emission-like ones.

In Figure 13 we compare the spectrum of Figure 12, calculated from a self-consistent velocity profile, to a spectrum based on the approximate velocity profile of equation (7). The flow velocity at the surface is $\beta_F = 0.26$ in the self-consistent calculation, compared with 0.50 in the approximation. Because of the smaller plasma velocity near the surface, the line centers are shifted closer to their rest frame values. In addition, the lines are considerably narrower in the self-consistent calculation. For $0 < \mu < \frac{1}{8}$ (panel a), $W_{E1} = 3.7$ keV in the self-consistent calculation, compared with 5.1 keV in the approximation. The reason for the narrower line is clear from equation (27), which shows that the plasma density $n_e(z)$ is proportional to the ratio $\beta_{Fo}/\beta_F(z)$. Figure 6 shows that this ratio is much smaller in self-consistent calculations. Consequently, for a given plasma density at $z = 0$, the plasma density at $z > 0$ is smaller in the self-consistent calculation, as is the optical depth.

Figure 14 compares the self-consistent calculation of Figure 13, which has temperature $k_B T_e = 0.25E_B$, to a calculation with $k_B T_e = 0.05E_B$. As we discuss in §§ 3.2 and 3.5, the effect of the temperature on the spectra is negligible for the parameters used here.

Figure 15 illustrates the effect of the surface electron density on the spectra. The figure shows the photon flux emerging from a line-forming region with $r_h = 0.05R_*$ and $B_{o,12} = 1.7$. The continuum spectrum of GRB 880205 is injected uniformly across the hot spot. The calculations include scattering in the continuum and the first three harmonics, finite natural line width, and a self-consistent velocity profile. The surface electron densities are $n_{e,o} = 10^{16}$, 10^{17}, and 10^{18} cm^{-3}. As expected, both the full-width half-maxima and $|W_E|$ increase with the plasma density. However, even at $n_{e,o} = 10^{18}$ cm^{-3}, the equivalent widths are modest, with $W_{E1} = 5.2$ and $W_{E2} = 7.9$ keV for $0 < \mu < \frac{1}{8}$.

We plot spectra from self-consistent calculations with *polarized* cross sections in Figure 16. The line-forming region has $r_h = 0.1R_*$, $B_{o,12} = 1.7$, and $n_{e,o} = 10^{17}$ cm^{-3}. The calculations include continuum and first three harmonic scattering with finite natural line width. The photons, injected uniformly across the hot spot and with the continuum spectrum of GRB 880205, have initial polarizations
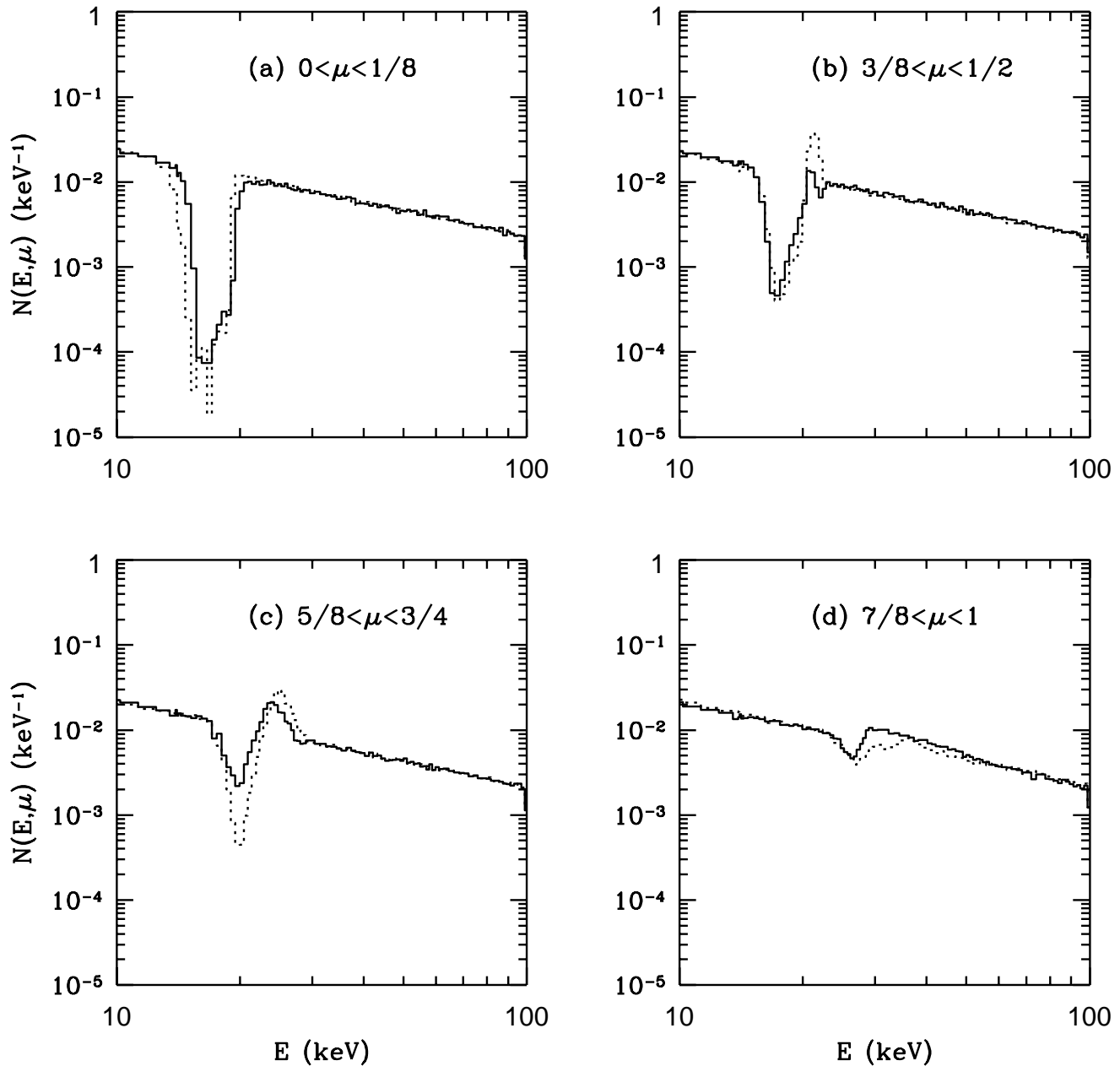
FIG. 10.—Effect of finite natural line width. Monte Carlo emerging photon number spectra for several viewing angles for a $1/E$ continuum spectrum injected at the origin of a hot spot with radius $r_h = 0.1R_*$. The line-forming region has dipole field $B_{o,12} = 1.7$, electron temperature $k_B T_e^f = 0.25E_B$, surface electron density $n_{e,o} = 10^{17}$ cm^{-3}, a self-consistent velocity profile, and unpolarized first harmonic scattering with finite (*solid lines*) and zero (*dotted lines*) natural line width.

$P_l = -1, 0$, and 1. The photons at the first harmonic scatter and switch polarization modes many times before escaping. Consequently, the properties of the first harmonic lines are not affected very much by the use of polarized cross sections or the choice of P_l. The scattering cross sections (eq. [40]) explain the properties of the higher harmonic features. Because of the μ^{r2} dependence of the cross section for parallel-mode photons, the second and third harmonic lines are very shallow near $\mu^r = 0$ (i.e., $\mu = \beta_{Fo} \approx 0.3$) when $P_l = -1$. The depth of the higher harmonic lines increases with the fraction of perpendicular-mode photons.

6. DISCUSSION

Fenimore et al. (1988) report that the two harmonically spaced lines observed by *Ginga* in GRB 880205 have equiv-

alent widths $W_{E1} = 3.7$ keV and $W_{E2} = 9.1$ keV. As we show in § 5, cyclotron scattering in an outflow can easily create lines with comparable equivalent widths, because of the escape of photons through the sides of the cylindrical line-forming region. For example, the first two harmonic lines in the spectrum in Figure 15b with $n_{e,o} = 10^{18}$ cm^{-3} and $3/8 < \mu < \frac{1}{2}$ have equivalent widths $W_{E1} = 2.3$ keV and $W_{E2} = 8.8$ keV. Clearly, the interpretation of the observed features as cyclotron lines does not rule out burst sources in the galactic corona, provided the photon source is a small fraction of the stellar surface. Thus, the cyclotron line interpretation is consistent with the BATSE brightness and sky distributions, which suggest that if bursters are galactic, they are in the corona. We are currently fitting the outflow model to the *Ginga* data in greater detail by folding the
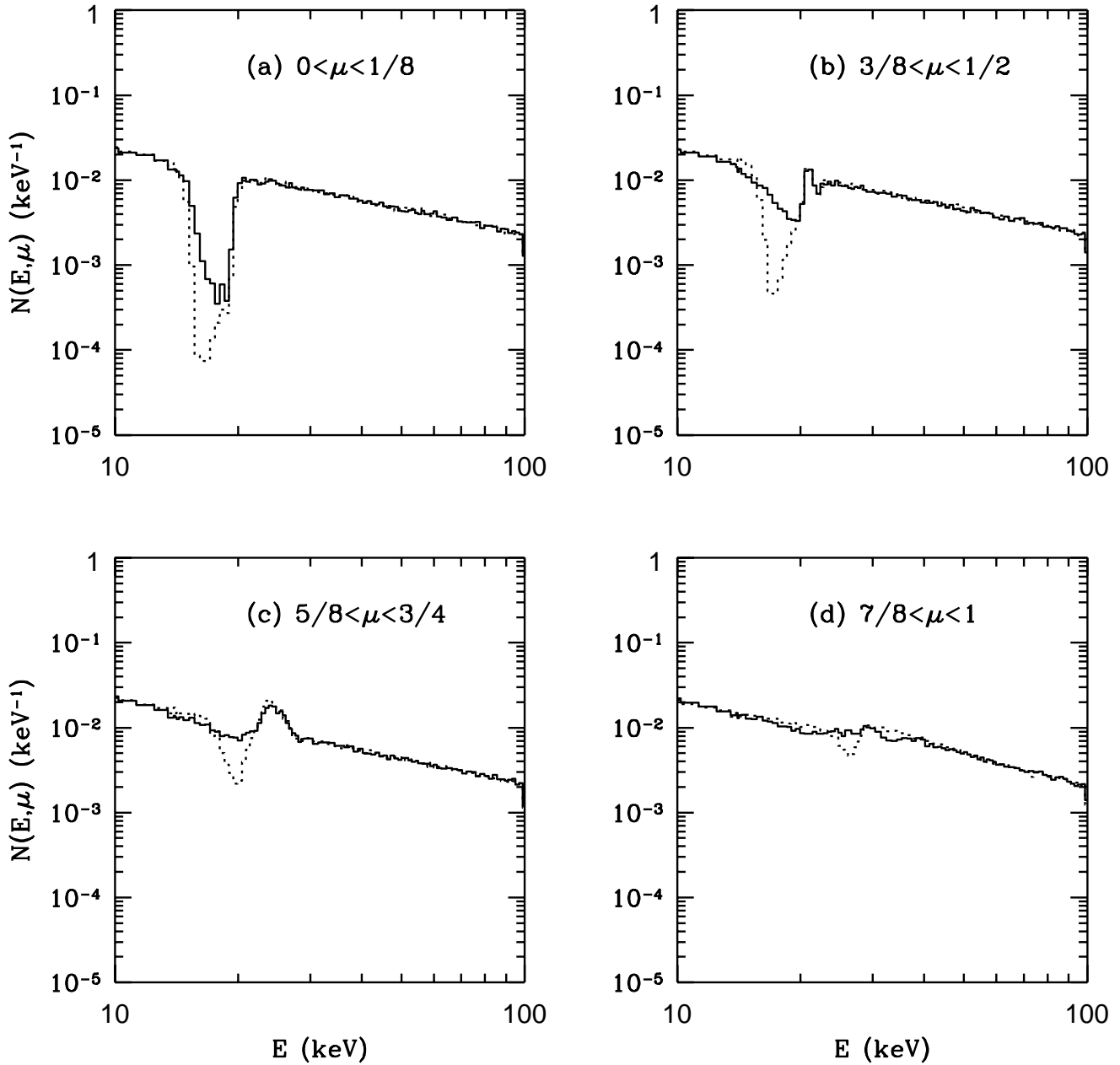
Fig. 11.—Effect of disk source. Monte Carlo emerging photon number spectra for several viewing angles for a $1/E$ continuum spectrum injected uniformly across a hot spot with radius $r_h = 0.1\ R_*$ (*solid lines*) and at the origin (*dotted lines*). The line-forming region has dipole field $B_{o,12} = 1.7$, electron temperature $k_B T_e^f = 0.25 E_B$, surface electron density $n_{e,o} = 10^{17}$ cm^{-3}, a self-consistent velocity profile, and unpolarized first harmonic scattering with finite natural line width.

model spectra through the detector response matrices and calculating χ^2 (see Fenimore et al. 1988; Wang et al. 1989; Briggs 1996).

In addition to generating cyclotron lines comparable to the absorption-like features observed by *Ginga*, the outflow model predicts the formation of emission-like features. Some static models predict double-peaked emission-like features, consisting of line shoulders on each side of an absorption-like line at certain viewing angles when the photon source is embedded in a plasma that is optically thin in the continuum (Freeman et al. 1992; Araya & Harding 1996; Isenberg et al. 1998). But these are quite distinct from the *single*-peaked features that the outflow model predicts. Mazets et al. (1981, 1982) report observations of such features by the KONUS instruments. The line candidates observed by BATSE (Briggs et al. 1996) also include

emission-like features. These observations should be compared to the model as soon as the observed spectra and detector response matrices become available.

All the simulations in the present work use plasma densities that are small enough so that the line-forming region is optically thin in the continuum, i.e., $n_e \lesssim \sigma_T^{-1} r_h^{-1} = 1.5 \times 10^{19}$ cm^{-3} $r_{h,5}^{-1}$. But for the physical conditions required for galactic corona models, the plasma density could be much larger due to the production of electron-positron pairs. The cross section for the two photon pair production process $\gamma\gamma \rightarrow e^+ e^-$ is $\sim \sigma_T$, corresponding to a pair production rate

$$R_{\gamma\gamma} \sim \frac{\sigma_T L}{\pi r_h^2 c \langle E \rangle} = 440 \text{ cm}^{-1}\ L_{42}\ r_{h,5}^{-2} \left(\frac{\langle E \rangle}{1 \text{ MeV}} \right)^{-1}, \quad (59)$$
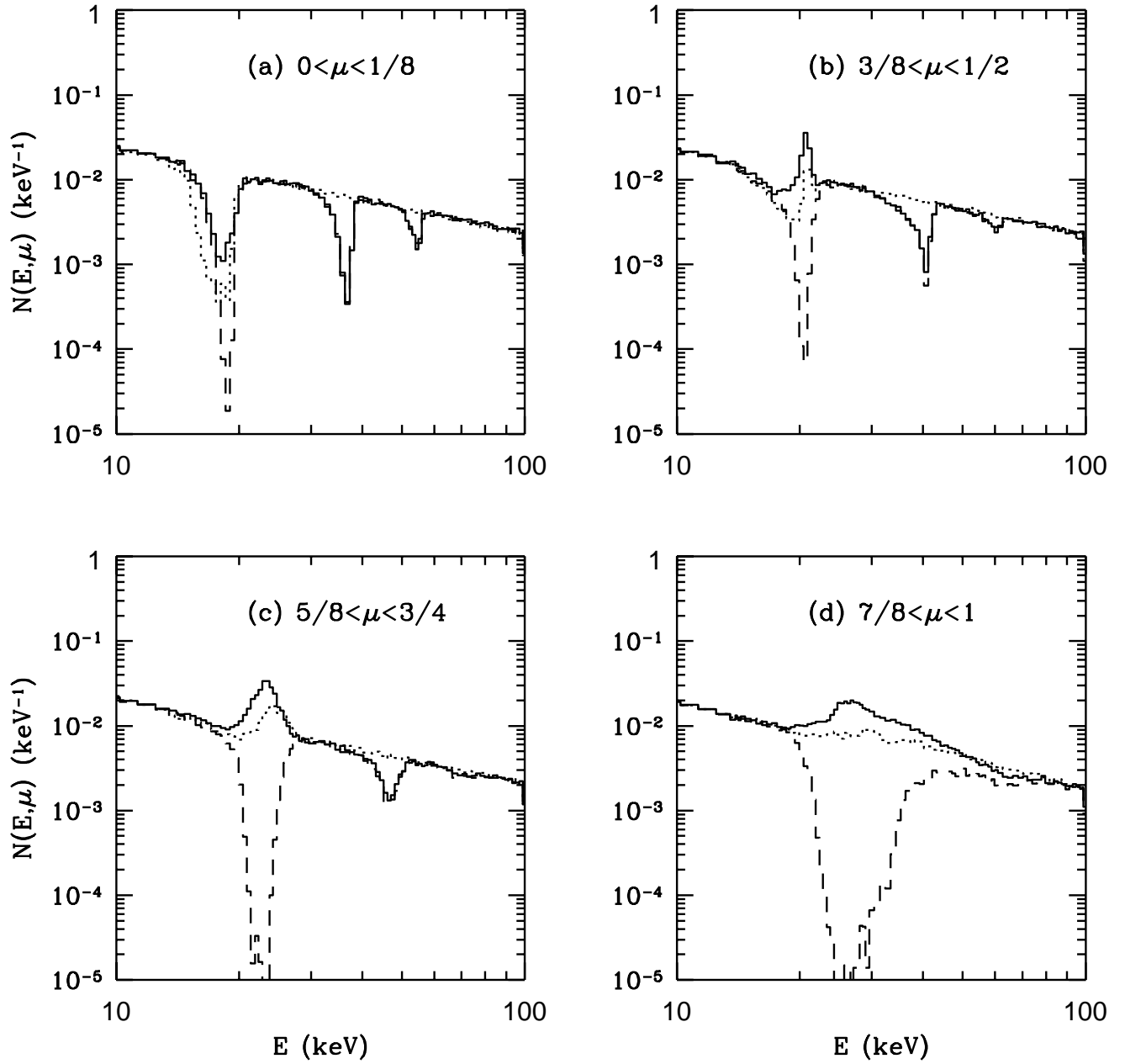
Fig. 12.—Effect of higher harmonic scattering. Monte Carlo emerging photon number spectra for several viewing angles for a $1/E$ continuum spectrum injected uniformly across a hot spot with radius $r_h = 0.1R_*$. The line-forming region has dipole field $B_{o,12} = 1.7$, electron temperature $k_B T_e^f = 0.25E_B$, surface electron density $n_{e,o} = 10^{17}$ cm^{-3}, a self-consistent velocity profile, and unpolarized continuum and first three harmonic scattering with finite natural line width (*solid lines*). Spectra for first harmonic scattering (*dotted lines*) and pure absorption (*dashed lines*) are shown for comparison.

where $L_{42} \equiv L/10^{42}$ ergs s^{-1} is the total (X-ray plus gamma ray) burst luminosity, and $\langle E \rangle$ is the mean photon energy. In a strong magnetic field, one photon pair production ($\gamma \rightarrow e^+ e^-$) is also significant. The polarization-averaged production rate for this process is

$$R_{\gamma B} \approx 0.26 \frac{\alpha}{\lambda_C} b \sin \theta \exp \left[-\frac{8}{3} \frac{m_e c^2}{Eb \sin \theta} \right]$$

$$= 1.1 \times 10^6 \text{ cm}^{-1} B_{12} \sin \theta$$

$$\times \exp \left[-6.1 \left(\frac{E}{10 \text{ MeV}} \right)^{-1} (B_{12} \sin \theta)^{-1} \right] \quad (60)$$

for $Eb \sin \theta/(m_e c^2) \ll 1$, and

$$R_{\gamma B} \approx \frac{5}{12} \frac{\alpha}{\lambda_C} \sin \theta \left(\frac{E}{m_e c^2} b \sin \theta \right)^{-1/3}$$

$$= 2.2 \times 10^7 \text{ cm}^{-1} \sin \theta \left(\frac{E}{1 \text{ GeV}} \right)^{-1/3} (B_{12} \sin \theta)^{-1/3}$$

$$(61)$$

for $Eb \sin \theta/(m_e c^2) \gg 1$, where $\lambda_C \equiv \hbar/(m_e c)$ is the Compton wavelength (Tsai & Erber 1974; Daugherty & Harding 1983; Burns & Harding 1984; Mészáros 1992). Clearly the optical depths for both the one and two photon processes
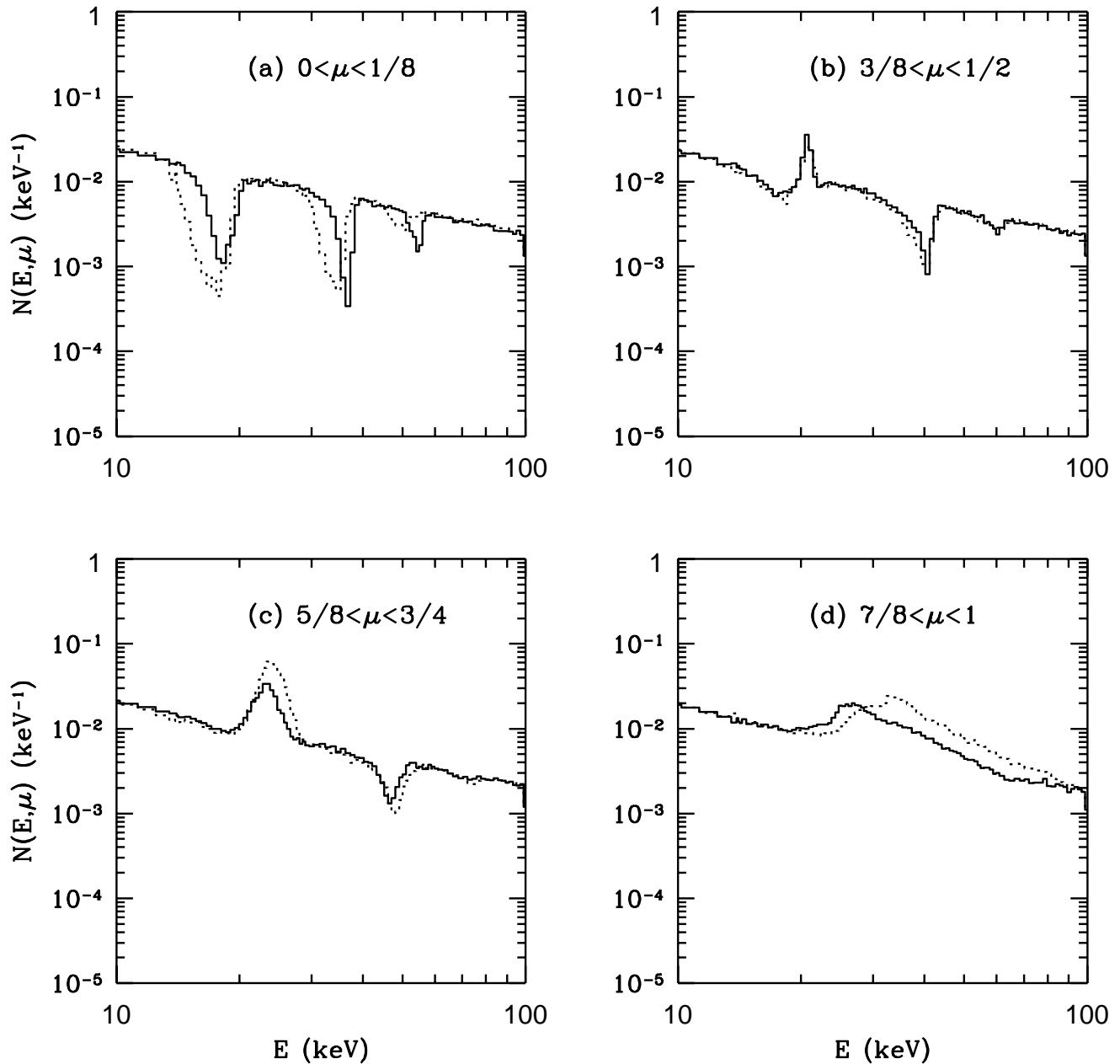
FIG. 13.—Monte Carlo emerging photon number spectra for several viewing angles for a $1/E$ continuum spectrum injected uniformly across a hot spot with $r_h = 0.1R_*$. The line-forming region has dipole field $B_{o,12} = 1.7$, electron temperature $k_B T_e^f = 0.25E_B$, surface electron density $n_{e,o} = 10^{17}$ cm^{-3}, unpolarized continuum and first three harmonic scattering with finite natural line width, and a self-consistent (*solid lines*) and $\beta_F = 0.5(1 + \mu_o)$ (*dotted lines*) velocity profile.

are much larger than unity for the magnetic fields and photons densities of interest in galactic corona gamma-ray burst models (Schmidt 1978; Brainerd & Lamb 1987). In addition to providing large plasma densities, pair production could truncate the spectrum at the pair production threshold, 1 MeV. Truncation is not consistent with observations by BATSE (Band et al. 1993), COMPTEL (Winkler et al. 1993), and EGRET (Schneid et al. 1992; Kwok et al. 1993; Sommer et al. 1994) of photon energies up to 1 GeV with no evidence of a spectral cutoff or rollover at ≈ 1 MeV.

The properties of lines formed in an outflow that is optically thick in the continuum are not very well known. The full-width half-maxima of the lines increase with optical depth like $(\ln \tau)^{1/2}$. This line broadening, though logarith-

mic, is significant if the plasma density increases by a factor $\gtrsim 100$; it might be sufficient to prevent the formation of narrow lines. However, parallel-mode photons with $\mu \approx \beta_F$ escape the line-forming region easily since their resonant scattering cross section is $\propto \mu^{r2}$. Therefore, the spectrum may possess narrow cyclotron features when viewed along this line of sight. The photon flux along this line of sight is about one-tenth the flux at $\mu = 1$ because nearly all photons scatter at these optical depths and are beamed along the field. Consequently, if the line of sight is at a large angle to the field, the observed flux is reduced and narrow lines are present. If the line of sight is at a small angle to the field, the observed flux is large. The absence of narrow features in gamma-ray burst spectra calculated from the "CUSP"
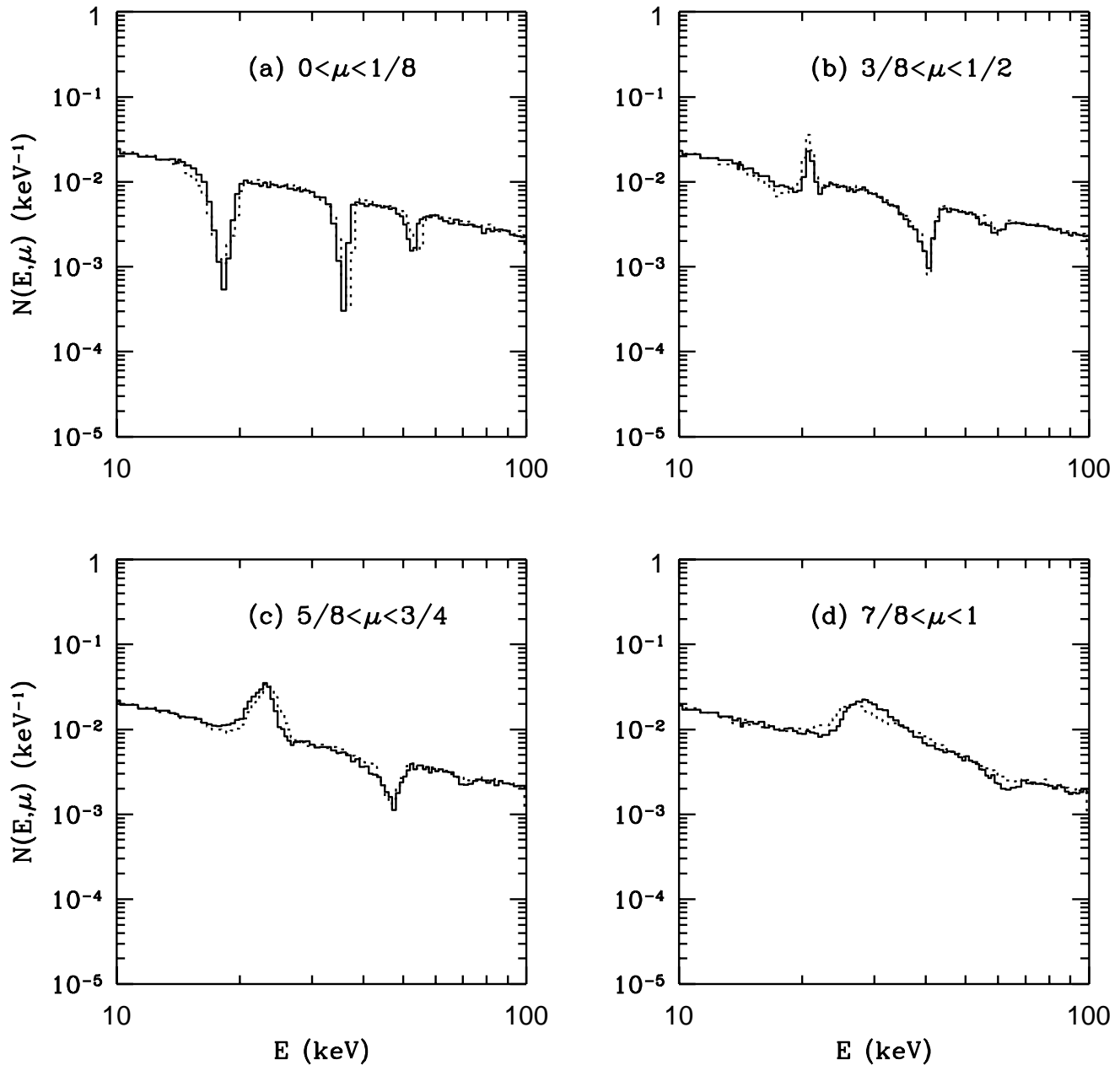
FIG. 14.—Effect of electron temperature. Monte Carlo emerging photon number spectra for several viewing angles for a $1/E$ continuum spectrum injected uniformly across a hot spot with radius $r_h = 0.1R_*$. The line-forming region has dipole field $B_{o,12} = 1.7$, surface electron density $n_{e,o} = 10^{17}$ cm^{-3}, a self-consistent velocity profile, unpolarized continuum and first three harmonic scattering with finite natural line width, and electron temperatures $k_B T_e^f = 0.05E_B$ (*solid lines*) and $0.25E_B$ (*dotted lines*).

model, in which the spectrum is formed by the Cyclotron Up Scattering Process (Vitello & Dermer 1991; Coppi & Lamb 1992), suggests that no narrow cyclotron feature is visible when the line of sight is at a small angle to the field. In short, if the cyclotron lines are formed in an outflow that is optically thick in the continuum, the presence of narrow lines is inversely correlated with the brightness of the burst. This correlation may be masked by selection effects: lines are easier to detect in brighter bursts. Whether spectra formed under these circumstances are consistent with observations is an open question. Additional simulations are required, using cross sections that are appropriate for plasmas that are optically thick in the line wings.

The plasma densities in corona models may be smaller than equations (59)–(61) suggest (for a review, see Higdon &

Lingenfelter 1990). One often cited possibility is that the entire photon spectrum is produced at the magnetic polar cap, but the photons are beamed into a small angle. Another is that the X-rays and gamma rays are produced in two separate physical regions, by two different mechanisms.

If a plasma with bulk motion corresponding to γ_F produces the spectrum, then the photons are beamed into an angle $\sim \gamma_F^{-1}$. The kinematics of two photon pair production requires $E_1 E_2(1 - \cos \theta_{12}) \geq 2m_e^2 c^4$, where E_1 and E_2 are the energies of the two photons and θ_{12} is the angle between them. A beaming angle ~ 0.1 (i.e., $\gamma_F \sim 10$) raises the pair production threshold enough to be consistent with the observed spectra above 1 MeV (Schmidt 1978; Baring & Harding 1993; Harding & Baring 1994; Harding 1994). Unfortunately, it is unlikely that the observed cyclotron
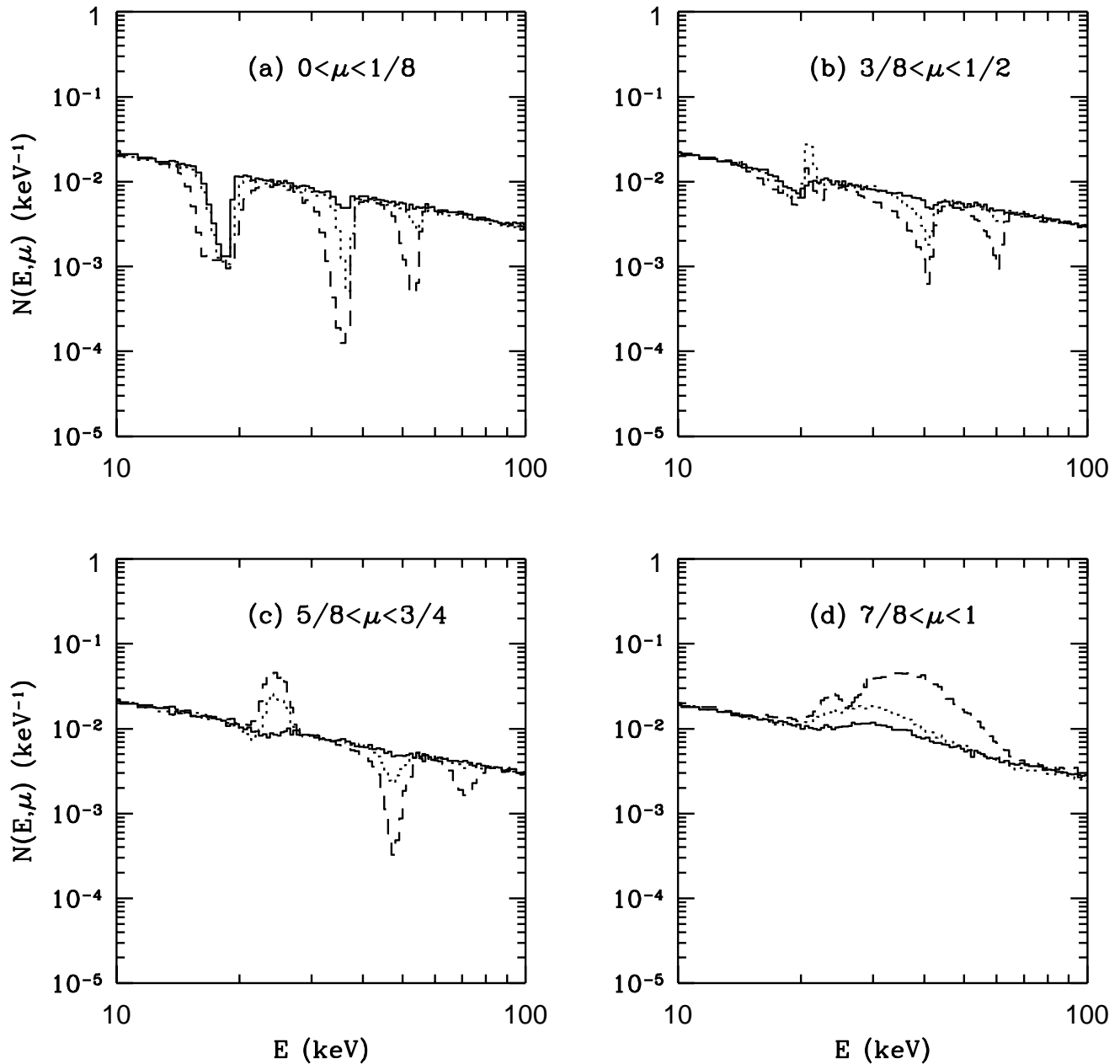
FIG. 15.—Effect of electron density. Monte Carlo emerging photon number spectra for several viewing angles for a GRB 880205 continuum spectrum injected uniformly across a hot spot with radius $r_h = 0.05R_*$. The line-forming region has dipole field $B_{o,12} = 1.7$, electron temperature $k_B T_e^f = 0.25E_B$, a self-consistent velocity profile, unpolarized continuum and first three harmonic scattering with finite natural line width, and surface electron densities $n_{e,o} = 10^{16}$ cm^{-3} (solid lines), $n_{e,o} = 10^{17}$ cm^{-3} (dotted lines), and $n_{e,o} = 10^{18}$ cm^{-3} (dashed lines).

features are produced in a plasma with such a large Lorentz factor. According to equation (30), the creation of a cyclotron first harmonic at 20 keV when $\gamma_F = 10$ and $\theta = 0.1$ requires a magnetic field $B_{12} \approx 0.2$, which is about an order of magnitude smaller than the fields we use in the present work. Since the ratio of the second and first harmonic scattering cross sections $\sigma_2/\sigma_1 \propto B$, the ratio W_{E2}/W_{E1} is much smaller for $B_{12} \approx 0.2$ than in the Ginga observations. To obtain the observed spectrum, the lines must be formed in a plasma in a separate location from the plasma responsible for beaming the radiation. The plasma in the line-forming region must also be moving more slowly than $\gamma_F = 10$.

This leads to the second possibility, that the gamma-ray burst spectrum consists of two components produced in two distinct physical regions: a soft ($E \lesssim 1$ MeV) com-

ponent produced near the magnetic pole and a hard component ($E \gtrsim 1$ MeV), probably produced at some distance above the surface (Lamb 1982; Katz 1982, 1994). If this is the case, then the photons in the line-forming region have energies below the pair production threshold and the plasma density can remain small. Since the region where the gamma rays are produced is larger and has a smaller magnetic field than in models where the gamma rays are produced at the polar cap, there is not sufficient pair production to truncate the spectrum at 1 MeV. A recent report by Chernenko & Mitrofanov (1995) of evidence for two components in the spectrum of GRB 881024 is intriguing. The soft component dominates the spectrum for $E < 250$ keV; the hard component is dominant at higher energies. However, the question of exactly where and how
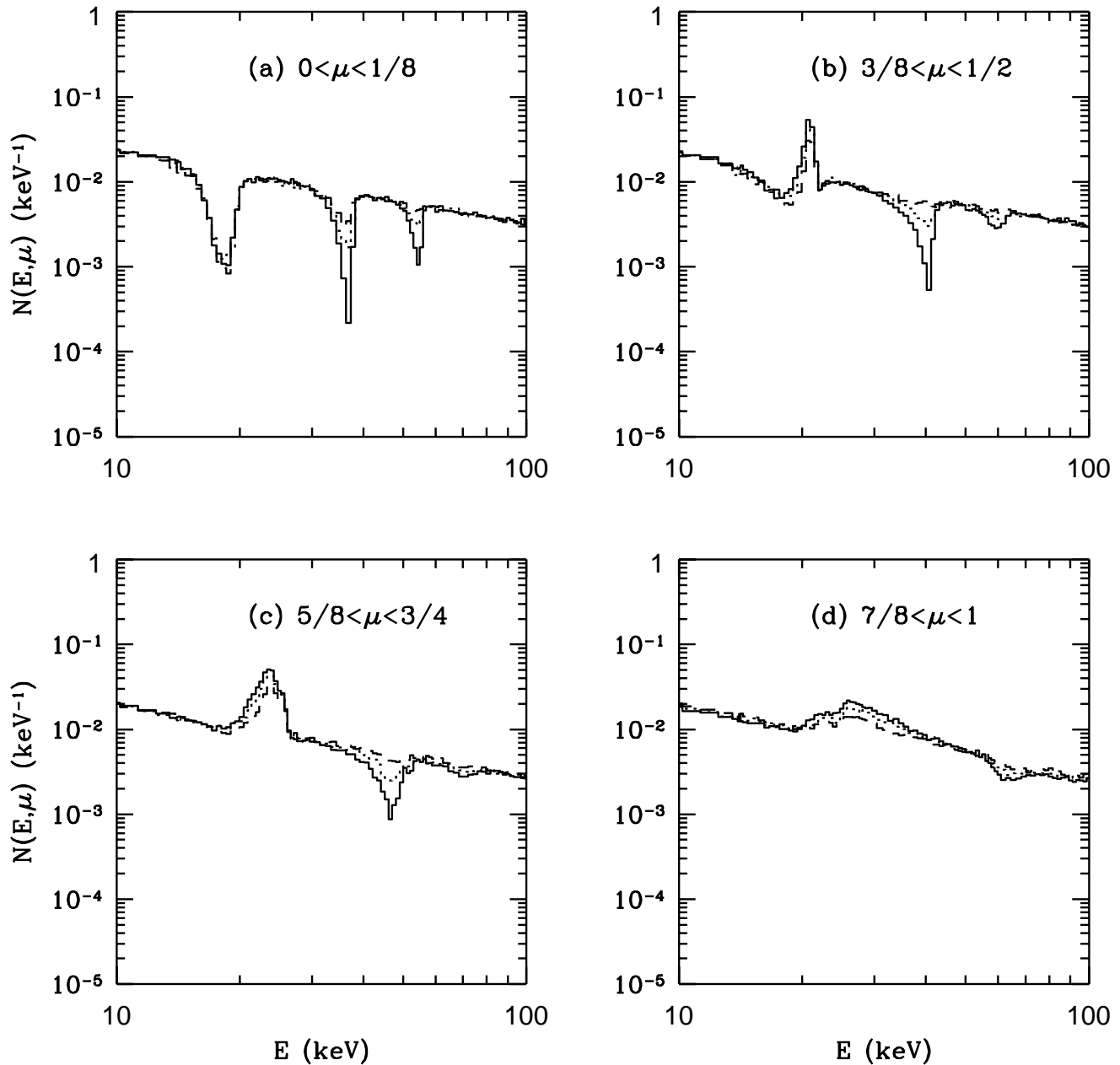
FIG. 16.—Effect of photon polarization. Monte Carlo emerging photon number spectra for several viewing angles for a GRB 880205 continuum spectrum injected uniformly across a hot spot with radius $r_h = 0.1 R_*$. The line-forming region has dipole field $B_{o,12} = 1.7$, electron temperature $k_B T_e^f = 0.25 E_B$, surface electron density $n_{e,o} = 10^{17}$ cm^{-3}, a self-consistent velocity profile, and polarized continuum and first three harmonic scattering with finite natural line width. The fraction of injected photons in parallel mode is $P_l = -1.0$ (*dashed lines*), 0.0 (*dotted lines*), and 1.0 (*solid lines*).

the high-energy component is produced remains open.

The cyclotron line interpretation of the observed spectral features strongly supports a galactic origin for at least some gamma-ray bursts. Recent reports of fading X-ray and optical counterparts apparently associated with GRB 970228 raise hopes that we will soon know the distance scale to the burst sources. If it turns out that some bursts are galactic, then our understanding of how cyclotron lines are formed at low energies will play an important role in constraining models of how the spectrum is formed at all energies.

We wish to thank Jeff Benensohn, Tomek Bulik, Peter Freeman, Carlo Graziani, Cole Miller, Guy Miller, Lucia

REFERENCES

Adler, S. L. 1971, Ann. Phys., 67, 599
Alexander, S. G., & Mészáros, P. 1989, ApJ, 344, L1
Araya, R. A., & Harding, A. K. 1996, ApJ, 463, 33
Band, D., et al. 1993, ApJ, 413, 281
Barat, C. 1993, A&AS, 97, 43
Baring, M. G., & Harding, A. K. 1993, in Proc. 23d Int. Cosmic-Ray Conf. (Calgary), 1, 53
Bonnell, J. T., & Klebesadel, R. W. 1996, in AIP Conf. Proc. 384, Gamma-Ray Bursts, 3d Huntsville Symposium, ed. C. Kouveliotou, M. S. Briggs, & G. J. Fishman (Woodbury: AIP), 977
Brainerd, J. J., & Lamb, D. Q. 1987, ApJ, 313, 231
Briggs, M. S. 1996, in AIP Conf. Proc. 384, Gamma-Ray Bursts, 3d Huntsville Symposium, ed. C. Kouveliotou, M. S. Briggs, & G. J. Fishman (Woodbury: AIP), 133
Briggs, M. S., et al. 1996, in AIP Conf. Proc. 384, Gamma-Ray Bursts, 3d Huntsville Symposium, ed. C. Kouveliotou, M. S. Briggs, & G. J. Fishman (Woodbury: AIP), 153
Burns, M. L., & Harding, A. K. 1984, ApJ, 285, 747
Bussard, R. W., & Lamb, F. K. 1982, in AIP Conf. Proc. 77, Gamma-Ray Transients and Related Astrophysical Phenomena, ed. R. E. Lingenfelter, H. S. Hudson, & Diana M. Worrall (New York: AIP), 189
Canuto, V., Lodenquai, J., & Ruderman, M. A. 1971, Phys. Rev. D, 3, 2303
Chanmugam, G. 1992, ARA&A, 30, 143
Chernenko, A., & Mitrofanov, I. 1993, in Isolated Pulsars, ed. K. A. Van Riper, R. Epstein, & C. Ho (Cambridge: Cambridge Univ. Press), 215
———. 1995, MNRAS, 274, 361
Clark, G. W., et al. 1990, ApJ, 353, 274
Coppi, P. S., & Lamb, D. Q. 1992, in AIP Conf. Proc. 265, Gamma-Ray Bursts, ed. W. S. Paciesas & G. J. Fishman (New York: AIP), 257
Costa, E., et al. 1997, IAU Circ., 6576
Daugherty, J. K., & Harding, A. K. 1983, ApJ, 273, 761
Daugherty, J. K., & Ventura, J. 1978, Phys. Rev. D, 18, 1053
de Haas, W. J., & van Alphen, P. M. 1930, Leiden Comm., 208d
Fenimore, E. E., et al. 1988, ApJ, 335, L71
Freeman, P. E., et al. 1992, in AIP Conf. Proc. 265, Gamma-Ray Bursts, ed. W. S. Paciesas & G. J. Fishman (New York: AIP), 216
———. 1996, in AIP Conf. Proc. 366, High Velocity Neutron Stars and Gamma-Ray Bursts, ed. R. E. Rothschild & R. E. Lingenfelter (New York: AIP), 211
Graziani, C. 1993, ApJ, 412, 351
Graziani, C., et al. 1992, in Gamma-Ray Bursts: Observations, Analyses, and Theories, ed. C. Ho, R. I. Epstein, & E. E. Fenimore (Cambridge: Cambridge Univ. Press), 407
Groot, P. J., et al. 1997a, IAU Circ., 6584
———. 1997b, IAU Circ., 6588
Grove, J. E., et al. 1995, ApJ, 438, L25
Harding, A. K. 1994, in AIP Conf. Proc. 304, The Second Compton Symposium, ed. C. Fichtel, N. Gehrels, & J. P. Norris (New York: AIP), 30
Harding, A. K., & Baring, M. G. 1994, in AIP Conf. Proc. 307, Gamma-Ray Bursts, Second Workshop, ed. G. J. Fishman, J. J. Brainerd, & K. Hurley (New York: AIP), 520
Harding, A. K., & Daugherty, J. K. 1991, ApJ, 374, 687
Harding, A. K., & Preece, R. D. 1989, ApJ, 338, L21
Herold, H. 1979, Phys. Rev. D, 19, 2868
Higdon, J. C., & Lingenfelter, R. E. 1990, ARA&A, 28, 401
Hueter, G. J. 1984, in AIP Conf. Proc. 115, High Energy Transients in Astrophysics, ed. S. E. Woosley (New York: AIP), 373
———. 1987, Ph.D. thesis, Univ. California, San Diego
Isenberg, M., Lamb, D. Q., & Wang, J. C. L. 1996, in AIP Conf. Proc. 384, Gamma-Ray Bursts, 3d Huntsville Symposium, ed. C. Kouveliotou, M. S. Briggs, & G. J. Fishman (Woodbury: AIP), 187
———. 1998, ApJ, submitted
Katz, J. I. 1982, ApJ, 260, 371
———. 1994, ApJ, 422, 248
Klebesadel, R. W., Strong, I. B., & Olson, R. A. 1973, ApJ, 182, L85
Kwok, P. W., et al. 1993, in AIP Conf. Proc. 280, Compton Gamma-Ray Observatory, ed. M. Friedlander, N. Gehrels, & D. J. Macomb (New York: AIP), 855

Lamb, D. Q. 1982, in Ann. NY Acad. Sci., 422, Proc. 11th Texas Symp. on Relativistic Astrophysics, ed. D. S. Evans, 237
———. 1995, PASP, 107, 1152
Lamb, D. Q., Wang, J. C. L., & Wasserman, I. 1990, ApJ, 363, 670
Lamb, D. Q., et al. 1989, in Ann. NY Acad Sci., 571, Proc. 14th Texas Symp. on Relativistic Astrophysics, ed. E. Fenyves, 460
Landau, L. D. 1930, Z. Phys, 64, 629
Landau, L. D., & Lifshitz, E. M. 1975, The Classical Theory of Fields (Oxford: Pergamon)
———. 1980, Statistical Physics, Part I (Oxford: Pergamon)
Langer, S. 1981, Phys. Rev. D., 23, 328
Makishima, K., & Mihara, T. 1992, in Frontiers of X-Ray Astronomy, ed. Y. Tanaka & K. Koyama (Tokyo: Universal Academy Press), 23
Mazets, E. P., et al. 1981, Nature, 290, 378
———. 1982, Ap&SS, 82, 261
———. 1983, in AIP Conf. Proc. 101, Positron-Electron Pairs in Astrophysics, ed. M. L. Burns, A. K. Harding, & R. Ramaty (New York: AIP), 36
Mazets, E. P., et al. 1996, in AIP Conf. Proc. 384, Gamma-Ray Bursts, 3d Huntsville Symposium, ed. C. Kouveliotou, M. S. Briggs, & G. J. Fishman (Woodbury: AIP), 492
Meegan, C., et al. 1996, IAU Circ., 6518
Mészáros, P. 1992, High Energy Radiation from Magnetized Neutron Stars (Chicago: Univ. Chicago Press)
Metzger, M. R., et al. 1997a, IAU Circ., 6588
———. 1997b, IAU Circ., 6631
Mihara, T. 1995, Ph.D. thesis, Univ. Tokyo
Miller, G. S., et al. 1991, Phys. Rev. Lett., 66, 1395
———. 1992, in Gamma-Ray Bursts: Observations, Analyses, and Theories, ed. C. Ho, R. I. Epstein, & E. E. Fenimore (Cambridge: Cambridge Univ. Press), 215
Mitrofanov, I. G., & Tsygan, A. I. 1982, Ap&SS, 84, 35
Murakami, T., et al. 1988, Nature, 335, 234
Nelson, R. W., Salpeter, E. E., & Wasserman, I. 1993, ApJ, 418, 874
Nishimura, O. 1994, PASJ, 46, 45
Nishimura, O., & Ebisuzaki, T. 1992, PASJ, 44, 109
Paczynski, B. 1995, PASP, 107, 1167
Rybicki, G. B., & Lightman, A. P. 1979, Radiative Processes in Astrophysics (New York: John Wiley)
Sahu, K., et al. 1997, IAU Circ., 6606
Schmidt, W. K. H. 1978, Nature, 271, 525
Schneid, E., et al. 1992, A&A, 255, L13
Sommer, M., et al. 1994, ApJ, 422, L63
Spitzer, L. 1962, Physics of Fully Ionized Gases (New York: Interscience)
Ternov, V. G., Begrov, V. G., & Zhukovskii, V. Ch. 1966, Moscow Univ. Bull., 21, 21
Trümper, J., et al. 1978, ApJ, 219, L105
Tsai, W., & Erber, T. 1974, Phys. Rev. D, 10, 492
Tsygan, A. I. 1981, Ap&SS, 77, 187
Ventura, J. 1979, Phys. Rev. D, 19, 1684
Visvanathan, N., & Wickramasinghe, D. T. 1979, Nature, 281, 47
Vitello, P., & Dermer, C. D. 1991, ApJ, 374, 668
Wang, J. C. L., et al. 1989, Phys. Rev. Lett., 63, 1550
Wang, J. C. L., Wasserman, I., & Lamb, D. Q. 1993, ApJ, 414, 815
Wang, J. C. L., Wasserman, I. M., & Salpeter, E. E. 1988, ApJS, 68, 735
Wang, Y.-M., & Frank, J. 1981, A&A, 92, 255
Wasserman, I., & Salpeter, E. 1980, ApJ, 241, 1107
Wheaton, W. A., et al. 1979, Nature, 282, 240
Winkler, C., et al. 1993, in AIP Conf. Proc. 280, Compton Gamma-Ray Observatory, ed. M. Friedlander, N. Gehrels, & D.J. Macomb (New York: AIP), 845
Yoshida, A., et al. 1992, in Gamma-Ray Bursts: Observations, Analyses, and Theories, ed. C. Ho, R. I. Epstein, & E. E. Fenimore (Cambridge: Cambridge Univ. Press), 399
Zheleznyakov, V. V., & Serber, A. V. 1994, Space Sci. Rev., 68, 275
———. 1995, Adv. Space Res., 16, 77